TU Delft

Delft University of Technology

Road map to L_4/L_5 with a solar sail

Farrés, Ariadna; Heiligers, Jeannette; Miguel, Narcís

DOI
10.1016/j.ast.2019.105458

Publication date
2019

Document Version
Accepted author manuscript

Published in
Aerospace Science and Technology

Citation (APA)
Farrés, A., Heiligers, J., & Miguel, N. (2019). Road map to L_4/L_5 with a solar sail. *Aerospace Science and Technology*, *95*, Article 105458. https://doi.org/10.1016/j.ast.2019.105458

Important note
To cite this publication, please use the final published version (if applicable).
Please check the document version above.

Copyright
Other than for strictly personal use, it is not permitted to download, forward or distribute the text or part of it, without the consent of the author(s) and/or copyright holder(s), unless the work is under an open content license such as Creative Commons.

Takedown policy
Please contact us and provide details if you believe this document breaches copyrights.
We will remove access to the work immediately and investigate your claim.

This work is downloaded from Delft University of Technology.
For technical reasons the number of authors shown on this cover page is limited to a maximum of 10.

Road Map to L_4/L_5 with a solar sail[1]

Ariadna Farrés[a,1], Jeannette Heiligers[b,1], Narcís Miguel[c,1]

[a]*Dr., Visiting Researcher, Goddard Planetary Heliophysics Institute, University of Maryland Baltimore County, 1000 Hilltop Circle, Baltimore, Maryland 21250.*
[b]*Dr., Marie Skłodowska-Curie Fellow, Delft University of Technology, Faculty of Aerospace Engineering, Kluyverweg 1, 2652 HS Delft.*
[c]*Dr., Postdoctoral Research Fellow, Politecnico di Milano, Department of Aerospace Science and Technology, Via La Masa 34, 20156, Milano.*

Abstract

This paper explores the capability of solar sails to transfer a probe from the displaced Sun-Earth L_1 and L_2 libration points to the region of practical stability (RPS) around the triangular equilibrium points L_4 and L_5. If the sailcraft arrives inside the RPS with zero synodical velocity, it will remain there with minor station keeping requirements. Moreover, the location of the RPS is ideal for space weather missions as the Sun can be observed from a different angle compared to spacecraft orbiting the L_1 point. The unstable manifolds of the displaced L_1 and L_2 points come close to these regions providing opportunities for natural transfer trajectories. By varying the solar sail orientation along the manifold, the dynamics can be altered and simple transfer trajectories that reach the RPS with few sail maneuvers are enabled. However, these trajectories are not optimal from a transfer time perspective, but can serve as suitable initial guesses for a direct optimization method to find minimum-time transfers between the displaced L_1 and L_2 points and the RPS at L_4 and L_5.

Keywords: solar sails, libration point orbits, invariant manifolds, regions of practical stability, minimum time optimization

Nomenclature

Constants

μ	Dimensionless Earth mass
σ^*	Critical sail loading
G	Universal gravitational constant
m_{sun}	Mass of the Sun
P_0	Solar radiation pressure at 1 astronomical unit
R_0	Sun-Earth distance equal to 1 astronomical unit

Other notation

$\ddot{\square}$	Second-order time derivative

[1]This paper was presented at the 2018 AIAA Science and Technology Forum in Kissimmee, Florida, January 8-12 2018.

Email addresses: ariadna.farresbasiana@nasa.gov (Ariadna Farrés), M.J.Heiligers@tudelft.nl (Jeannette Heiligers), narcis.miguel@polimi.it (Narcís Miguel)

$\Delta\square$ Difference

$\dot{\square}$ First-order time derivative

Paramters

α Pitch angle

β Lightness number

δ Clock angle

ρ_a Absorption coefficient

ρ_s Reflectivity coefficient

σ Ratio of spacecraft mass and sail area

A Solar sail area

a_0 Characteristic acceleration

m Spacecraft mass

P Solar radiation pressure

Subscripts

$_0$ Initial

$_f$ Final

$_i$ Integer with $i = 1, 2, \ldots$

$_M$ Maximal

$_m$ Minimal

$_R$ Related to region $\mathcal{R}$

$_{max}$ Maximum

Variables

(r, θ) Polar coordinates

(x, y, z) Axes of synodical reference frame

$\mathbf{k}$ Vector of static parameters

$\hat{\mathbf{n}} = (n_x, n_y, n_z)$ Solar sail unit normal vector

$\hat{\mathbf{r}}_s$ Sun-sail unit vector

$\hat{\mathbf{z}}$ Unit vector along z-axis

$\Omega(x, y, z)$ Sum of gravitational and centripetal potential

$\{\hat{\mathbf{r}}_s, \hat{\mathbf{p}}, \hat{\mathbf{q}}\}$ Sail-centered reference frame to define solar sail acceleration vector

J Objective function

J_c Jacobi constant

R, R' Subset in (x, y)- or (r, θ)-coordinates around $SL_{4,5}$

r_2 Sun-sail distance projected on (x, y)-plane

R_S Distance from the Sun

r_{pe} Earth-sail distance

r_{ps} Sun-sail distance

SL_i Displaced Libration point with $i = 1, \ldots, 5$

T Integration time

t Time

u Control variable

$W^s(SL_i)$ Stable manifold of the displaced SL_i point with $i = 1, 2$

$W^u(SL_i)$ Unstable manifold of the displaced SL_i point with $i = 1, 2$

$\hat{\mathbf{v}}_i^u$ Unstable direction of the SL_i equilibrium point

$\mathbf{a}_s = (a_x, a_y, a_z)$ Solar sail acceleration vector and components

$\mathbf{F}_a$ Solar radiation pressure force due to absorption

$\mathbf{F}_r$ Solar radiation pressure force due to reflection

$\mathbf{r}_{pe}$ Earth-sail vector

$\mathbf{r}_{ps}$ Sun-sail vector

1. Introduction

Solar sails are a type of low-thrust propulsion system that take advantage of the Solar Radiation Pressure (SRP) to accelerate a probe by means of a highly reflective surface. To date, there have been three successful solar sail demonstration missions: IKAROS by JAXA (May 2010)[41], NanoSail-D2 by NASA (December 2010)[21] and LightSail-1 by The Planetary Society (June 2016)[39]. These successes have sparked further interest in solar sailing, resulting in more scheduled demonstration missions in the upcoming two years: LightSail-2 (the follow-up of LightSail-1 by The Planetary Society) and NASA's NEA Scout mission.

The unique selling point of solar sailing is the fact that its propulsive capabilities do not rely on an on-board reaction mass. This makes solar sailing an appealing option for a range of challenging mission concepts such as hovering along the Sun-Earth line sunward of the L_1 point (also known as the Geostorm [44, 42] or Sunjammer mission concept [18, 19]), displacing the orbits or L_1 point above the ecliptic plane for high-latitude observations of the Earth [30, 13, 11], precising an elliptical Earth-centered orbit for long residence times in the Earth's magnetotail (the GeoSail mission concept [25, 28, 32]), and even low-cost multi-asteroid rendezvous missions [33]. The purpose of the current paper is to complement this extensive list of solar sail enabled mission concepts with a preliminary study on the feasibility of solar sail transfers from the L_1 and L_2 points of the Sun-Earth Circular Restricted Three Body Problem (CRTBP) to the vicinity of the L_4 and L_5 points.

The Sun-Earth CRTBP is a well-known reference model in astrodynamics and has been extensively studied in the past [40]. It is also well-known that the system exhibits five equilibrium points $(L_1, \ldots, L_5)$ whose position can be artificially displaced when including a solar sail acceleration [27]. Due to their strategic location close to the Earth and their dynamical properties, periodic and quasi-periodic orbits around L_1

and L_2 have been used as reference orbits for several mission in the past such as SOHO, Genesis, GAIA, and Hershel-Plank. Because orbits around L_4 and L_5 are stable and no station keeping is required, they are also starting to become of interest. Besides the interest from an astrodynamics perspective, the L_4 and L_5 points also hold great scientific interest as they provide a unique "side-on" view of the Sun. Such a view would be crucial in furthering the understanding of the initiation and propagation of space weather events as well as improving current space weather event forecasting capabilities. In particular, through the side-on view, the speed of Coronal Mass Ejections (CMEs) can be measured with greater accuracy and, from L_5, the part of the Sun's surface that is about to rotate towards the Earth can be observed providing an early view of the CMEs [14].

Though of significant interest, the L_4 and L_5 points are hard to reach, but recent studies [35, 6] show that with solar sail propulsion, the vicinity of the L_4 and L_5 points can be reached in a reasonable amount of time. While the work by Sood and Howell [35] (and a similar work for chemical propulsion by Llanos et al. [24]), proposes to depart from a parking orbit around the Earth and reach a stable periodic orbit around L_4/L_5, the goal of the current paper is to use the natural dynamics of the system; in particular, taking advantage of the invariant manifold structure around L_1 and L_2 [22] to design transfer trajectories to the Regions of Practical Stability (RPS) around L_4/L_5 [36, 37]. These regions are ideal final destinations, as the trajectory of a probe starting inside these regions with zero synodic velocity will not escape within 1000 years. To obtain time-optimal transfers to these regions, we employ a two-step approach. The first step consists of generating transfer trajectories from the vicinity of L_1 and L_2 to a suitable neighborhood of the L_4/L_5 points by means of the unstable invariant manifolds of the former equilibria. These trajectories are sub-optimal from a transfer-time perspective due to the assumptions made during the design process. However, they are excellent initial guesses to solve the optimal control problem associated with finding time-optimal transfers between L_1/L_2 and the L_4/L_5 RPS. The second step consists of solving the optimal control problem using the software tool PSOPT [1], which is a particular implementation of a direct pseudo-spectral method in C^{++}. In both steps we consider the classical CRTBP as the dynamical model, accounting for SRP acting on the solar sail (CRTBPS from now on), where the sail acceleration depends on three parameters: the sail lightness number, β, (accounting for the sail efficiency), and two angles, α and δ (accounting for the sail orientation).

This paper is organized as follows: Section 2 introduces the CRTBPS and describes the main parameters of the system (β, α and δ). Section 3 describes the non-linear dynamics around the two regions that play an important role during the design process of the transfer trajectories: the invariant manifold structure around the displaced L_1 and L_2 equilibrium points (subsection 3.1) and the region of practical stability around L_4/L_5 (subsection 3.2). Section 4 addresses the main goal of the paper, finding transfer trajectories between L_1/L_2 and L_4/L_5, where subsection 4.1 explains how we explore the phase space to find a piece-wise transfer trajectory and subsection 4.2 takes these initial guesses to find time-optimal transfers. Finally, the conclusions are given at the end of the paper in Section 5.

2. Equations of Motion

To model the motion of a solar sail in the Sun - Earth system the CRTBPS is considered. Let us recall that the CRTBPS assumes that both Earth and Sun are point masses that move around their common center of mass in a circular way due to their mutual gravitational attraction. The solar sail, on the other hand, is a mass-less particle that does not affect the motion of both primaries, but is affected by their gravitational attraction as well as SRP.

The units of mass, distance and time are normalized so that the total mass of the system is 1, the Sun - Earth distance is 1 and the period of its orbit is 2π. In these units the Earth's mass is $\mu = 3.0034806 \times 10^{-6}$, and $1 - \mu$ corresponds to the Sun's mass. A synodical reference system is considered with its origin at the Sun - Earth system center of mass, and having Earth and Sun fixed on the x-axis (with the positive x-axis pointing from the Sun to the Earth). The z-axis is perpendicular to the ecliptic plane and the y-axis completes an orthogonal positive oriented reference system [40]. On the left panel of Figure 1 a schematic representation of the main forces in the CRTBPS is provided.

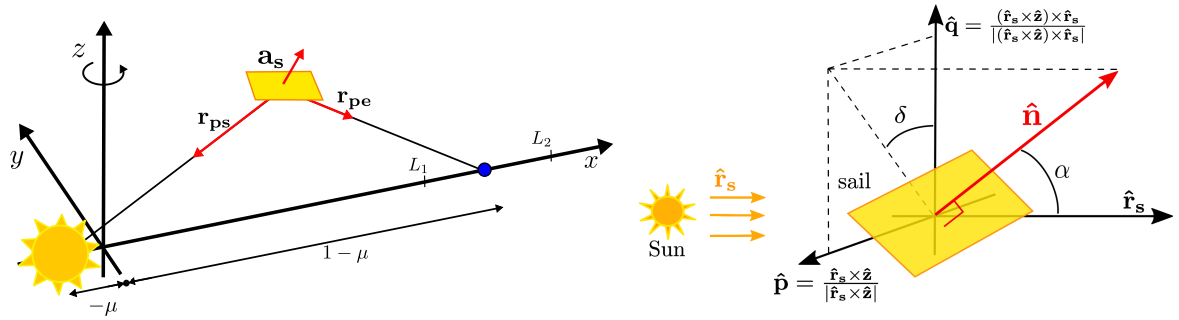

Figure 1: Left: Schematic representation of the CRTBPS model. Right: Schematic representation of the reference frame used to define the pitch and clock angles α and δ, respectively.

With these assumptions, the equations of motion in the synodical reference frame are:

$$\ddot{x} - 2\dot{y} = \frac{\partial \Omega}{\partial x} + a_x, \qquad \ddot{y} + 2\dot{x} = \frac{\partial \Omega}{\partial y} + a_y, \qquad \ddot{z} = \frac{\partial \Omega}{\partial z} + a_z, \tag{1}$$

where $\Omega(x,y,z) = \frac{1}{2}(x^2+y^2) + \frac{1-\mu}{r_{ps}} + \frac{\mu}{r_{pe}}$ while $r_{ps} = \sqrt{(x+\mu)^2+y^2+z^2}$ and $r_{pe} = \sqrt{(x+\mu-1)^2+y^2+z^2}$ are the Sun-sail and Earth-sail distances, respectively, and $\mathbf{a_s} = (a_x, a_y, a_z)$ is the acceleration due to the solar sail. The solar sail acceleration $\mathbf{a_s}$ depends on the sail's reflectivity properties, given by the lightness number (β) and the reflectivity coefficient (ρ_s); and the solar sail's orientation, which is determined by the pitch and clock angles (α and δ, respectively). A further detailed discussion on these parameters is given in the next subsection.

2.1. Solar Sail Acceleration

The solar sail acceleration is produced by the impact of the photons emitted by the Sun on the surface of the sail, which are reflected and absorbed by the sail material [27, 3]. For a solar sail with an area A, the force due to the reflection of photons is given by $\mathbf{F_r} = 2PA\langle \hat{\mathbf{r}}_\mathbf{s}, \hat{\mathbf{n}}\rangle^2 \hat{\mathbf{n}}$ while the force due to absorption is $\mathbf{F_a} = PA\langle \hat{\mathbf{r}}_\mathbf{s}, \hat{\mathbf{n}}\rangle \hat{\mathbf{r}}_\mathbf{s}$. Where $\hat{\mathbf{r}}_\mathbf{s} = (x+\mu, y, z)/r_{ps}$ is the Sun-sail direction, $\hat{\mathbf{n}}$ is the external normal direction to the sail (both unit vectors), and $P = P_0(R_0/R_S)^2$ is the SRP at a distance R_S from the Sun (where $P_0 = 4.563$ N/m^2 is the SRP at $R_0 = 1$ AU). If we denote ρ_a as the absorption coefficient and ρ_s as the reflectivity coefficient (which satisfy $\rho_a + \rho_s = 1$), the solar sail acceleration on a spacecraft of mass m is given by:

$$\mathbf{a_s} = \frac{2PA}{m}\langle \hat{\mathbf{r}}_\mathbf{s}, \hat{\mathbf{n}}\rangle \left(\rho_s \langle \hat{\mathbf{r}}_\mathbf{s}, \hat{\mathbf{n}}\rangle \hat{\mathbf{n}} + \frac{1}{2}(1-\rho_s)\hat{\mathbf{r}}_\mathbf{s} \right). \tag{2}$$

Note that $\rho_s = 1$ corresponds to a perfectly reflecting solar sail and $\rho_s = 0$ to a perfect solar panel where the photons are absorbed. According to [31, 17, 16] , a solar sail with a highly reflective aluminum-coated side has an estimated reflectivity coefficient of $\rho_s \approx 0.88$. However, in this paper the solar sail is assumed to be flat and perfectly reflecting ($\rho_s = 1$). In future studies more accurate models for the solar sail acceleration including imperfections of the solar sail material will be considered, to allow an assessment of how this affects the transfer trajectories.

2.1.1. Sail Lightness Number

Notice that SRP is proportional to the inverse square of the distance to the Sun (i.e., $P = P_0(R_0/R)^2$). Therefore it is common to rewrite the term $2PA/m$ in Eq. 2 as a correction of the Sun's gravitational

attraction: $\beta(1-\mu)/r_{ps}^2$, where β corresponds to the sail lightness number and accounts for the sail's efficiency. Following McInnes [27] it can be seen that, $\beta = \sigma^*/\sigma$, where $\sigma^* = 2P_0R_0^2/(Gm_{sun}) = 1.53$ g/m^2 (with G the universal gravitational constant and m_{sun} the mass of the Sun) and $\sigma = m/A$ is the solar sail mass-to-area ratio. The parameter β can then be seen as the ratio between the maximum propulsive acceleration generated by the sail at a given heliocentric distance (i.e. with a Sun-facing attitude) and the local Sun gravitational attraction. Another parameter used to describe the sail efficiency is through the characteristic acceleration (a_0), which represents the acceleration experienced by the sailcraft at 1 AU when the sail is oriented perpendicular to the Sun-sail line. The characteristic acceleration and the sail lightness number are related by: $a_0 = \beta G m_{sun}/R_0^2$.

Table 1 presents, for different values of the sail lightness number (β), the corresponding mass-to-area ratio (σ), the characteristic acceleration (a_0) and the required solar sail size for a 10 kg sailcraft. The near-term solar sail demonstration missions LightSail-1 and NEA-Scout (will) achieve a sail lightness number of $\beta = 0.011$[2] [2] and $\beta = 0.01$ [38], respectively, while future mission concepts like the Geostorm or Sunjammer concepts may achieve $\beta = 0.036$ [18].

Table 1: Relation between the sail lightness number β and the satellite's mass-to-area ratio (σ), the characteristic acceleration (a_0), and the required sail area for a satellite with 10 kg of total mass.

β	σ (g/m^2)	a_0 (mm/s^2)	Area (m^2)
0.01	153.0	0.059935	$\approx 8 \times 8$
0.02	76.5	0.119869	$\approx 12 \times 12$
0.03	51.0	0.179804	$\approx 14 \times 14$
0.04	38.25	0.239739	$\approx 16 \times 16$
0.05	30.6	0.359608	$\approx 20 \times 20$

2.1.2. Sail Orientation

The sail orientation is given by the normal direction to the surface of the sail ($\hat{\mathbf{n}}$) and is parameterised by two angles α and δ that measure the displacement between $\hat{\mathbf{n}}$ and $\hat{\mathbf{r}}_\mathbf{s} = (x-\mu, y, z)/r_{ps}$. Following McInnes [26], the orthonormal reference frame $\{\hat{\mathbf{r}}_\mathbf{s}, \hat{\mathbf{p}}, \hat{\mathbf{q}}\}$ centered at the sailcraft center of mass is considered (where $\hat{\mathbf{p}} = \frac{\hat{\mathbf{r}}_\mathbf{s}\times\hat{\mathbf{z}}}{|\hat{\mathbf{r}}_\mathbf{s}\times\hat{\mathbf{z}}|}$, $\hat{\mathbf{q}} = \frac{(\hat{\mathbf{r}}_s\times\hat{\mathbf{z}})\times\hat{\mathbf{r}}_\mathbf{s}}{|(\hat{\mathbf{r}}_\mathbf{s}\times\hat{\mathbf{z}})\times\hat{\mathbf{r}}_\mathbf{s}|}$ and $\hat{\mathbf{z}} = (0,0,1)$) and the normal vector to the sail is defined as $\hat{\mathbf{n}} = \cos\alpha\ \hat{\mathbf{r}}_\mathbf{s} + \sin\alpha\cos\delta\ \hat{\mathbf{q}} + \sin\alpha\sin\delta\ \hat{\mathbf{p}}$. With this definition α corresponds to the pitch angle (angle between $\hat{\mathbf{n}}$ and $\hat{\mathbf{r}}_\mathbf{s}$) and δ to the clock angle (angle between $\hat{\mathbf{q}}$ and the projection of $\hat{\mathbf{n}}$ on a plane orthogonal to $\hat{\mathbf{r}}_\mathbf{s}$). Figure 1 (right) shows a schematic representation of the definition of these two sail angles.

Finally, following these definitions, the explicit expressions for the normal vector to the surface of the solar sail, $\hat{\mathbf{n}} = (n_x, n_y, n_z)$, are:

$$\begin{aligned} n_x &= \frac{x-\mu}{r_{ps}}\cos\alpha - \frac{(x-\mu)z}{r_2 r_{ps}}\sin\alpha\cos\delta + \frac{y}{r_2}\sin\alpha\sin\delta, \\ n_y &= \frac{y}{r_{ps}}\cos\alpha - \frac{yz}{r_2 r_{ps}}\sin\alpha\cos\delta - \frac{x-\mu}{r_2}\sin\alpha\sin\delta, \\ n_z &= \frac{z}{r_{ps}}\cos\alpha + \frac{r_2}{r_{ps}}\sin\alpha\cos\delta, \end{aligned} \tag{3}$$

where $r_2 = \sqrt{(x-\mu)^2 + y^2}$. Notice that $\hat{\mathbf{n}}$ cannot point towards the Sun, hence $\langle\hat{\mathbf{n}}, \hat{\mathbf{r}}_\mathbf{s}\rangle = \cos\alpha \geq 0$, which implies that $\alpha \in [-\pi/2, \pi/2]$ while $\delta \in [0, \pi]$.

2.2. Properties of the CRTBPS

From a mathematical perspective, the Sun - Earth - sail CRTBPS is a perturbation of the Sun - Earth CRTBP, where the perturbation depends on the sail parameters $(\beta, \rho_s, \alpha, \delta)$. For a perfectly reflecting solar

[2]ESA eoPortalDirectory, LightSail-1, https://earth.esa.int/web/eoportal/satellite-missions/l/lightsail-1, Accessed 12 April 2019

sail ($\rho_s = 1$), Eq. 1 can be rewritten as [26, 5]:

$$\begin{aligned}
\ddot{x} - 2\dot{y} &= \frac{\partial \tilde{\Omega}}{\partial x} + \beta \frac{1-\mu}{r_{ps}^2} \cos^2\alpha \left(\frac{-(x-\mu)z}{r_2 r_{ps}} \sin\alpha\cos\delta + \frac{y}{r_2} \sin\alpha \sin\delta \right), \\
\ddot{y} + 2\dot{x} &= \frac{\partial \tilde{\Omega}}{\partial y} + \beta \frac{1-\mu}{r_{ps}^2} \cos^2\alpha \left(\frac{-yz}{r_2 r_{ps}} \sin\alpha\cos\delta - \frac{x-\mu}{r_2} \sin\alpha \sin\delta \right), \\
\ddot{z} &= \frac{\partial \tilde{\Omega}}{\partial z} + \beta \frac{1-\mu}{r_{ps}^2} \cos^2\alpha \left(\frac{r_2}{r_{ps}} \sin\alpha\cos\delta \right),
\end{aligned} \tag{4}$$

where $\tilde{\Omega}(x,y,z) = \frac{1}{2}(x^2+y^2) + (1-\beta\cos^3\alpha)\frac{1-\mu}{r_{ps}} + \frac{\mu}{r_{pe}}$.

It is well-known that the classical CRTBP (no solar sail) is Hamiltonian, but when the perturbation due to the solar sail is included, the Hamiltonian structure of the system breaks down unless $\alpha = 0$ (i.e., the solar sail is oriented perpendicular to the Sun-sail line) or $\alpha = \pm\pi/2$ (i.e., no sail effect). Furthermore, the system is time reversible for $\alpha \neq 0, \delta = 0$ (i.e., the orientation of the solar sail varies vertically with respect to the Sun-sail line) [8, 5]. In these two particular cases, for a fixed sail orientation, the Lyapunov Center Theorem for reversible systems ensures the existence of families of periodic and quasi-periodic orbits around an equilibrium point [34, 23].

As in the CRTBP, one can define the Jacobi function as:

$$J_c = \dot{x}^2 + \dot{y}^2 + \dot{z}^2 - 2\tilde{\Omega}(x,y,z), \tag{5}$$

where for $\beta = 0$ (i.e., no sail) and for $\beta \neq 0, \alpha = 0$ (a sail perpendicular to the Sun-sail line), this function corresponds to the Jacobi constant of the CRTBP or CRTBPS (Hamiltonian case). If $\alpha \neq 0$ this function is not constant but it can still be used to classify types of motion [7, 8].

Let us note that the system also has the following symmetries:

$$\begin{aligned}
S1 &: (t,\ x,\ y,\ z,\ \alpha,\ \delta) \mapsto (-t,\ x,\ -y,\ -z,\ -\alpha,\ \ \delta), \\
S2 &: (t,\ x,\ y,\ z,\ \alpha,\ \delta) \mapsto (-t,\ x,\ -y,\ \ \ z,\ \ \ \alpha,\ -\delta),
\end{aligned} \tag{6}$$

which can be useful to reduce the search space, when computing equilibrium points and periodic orbits or when describing the systems dynamics.

2.2.1. Equilibrium Points

It is well-known that when SRP is discarded ($\beta = 0$) the Sun - Earth CRTBP has five equilibrium points [40], and that all of them lie in the ecliptic plane ($z = 0$). Three of them, known as the *collinear points* $L_{1,2,3}$, lie on the line joining the two primaries ($y = 0$). The other two, known as the *triangular points* $L_{4,5}$, lie in the ecliptic plane, and form an equilateral triangle with the two primaries (i.e., their distance to both Earth and Sun is 1). The three collinear points are all linearly unstable (saddle×center×center), whereas the two triangular points are linearly stable (center×center×center).

If the sail is oriented perpendicular to the Sun-sail line ($\alpha = 0$) the system presents a similar phase space portrait as for $\beta = 0$: there are also five equilibrium points $SL_{1,\ldots,5}$ in the ecliptic plane, siblings to the classical $L_{1,\ldots,5}$ which are displaced towards the Sun [26]. The three collinear points ($SL_{1,2,3}$) still lie on the Sun - Earth line, and are linearly unstable (saddle×center×center). However, the two triangular points ($SL_{4,5}$) no longer form an equilateral triangle. While their distance to the Earth is always 1, the distance to the Sun is a function of the parameter β, namely $(1-\beta)^{1/3}$. However, $SL_{4,5}$ are also linearly stable for all β.

Recall that there is no explicit expression for the three collinear equilibrium points, but that their position can be found by solving a quintic. Defining, $\gamma_{1,2}$ as the distance from $SL_{1,2}$ to the Earth, and γ_3 as the distance from SL_3 to the Sun, it can be seen that the γ_i are the only positive solution to the quintic equations [40, 26]:

$$\gamma_1^5 + (3-\mu)\gamma_1^4 + (3-2\mu)\gamma_1^3 - (\mu\beta - \beta + \mu)\gamma_1^2 - 2\mu\gamma_1 - \mu = 0, \tag{7}$$

$$\gamma_2^5 - (3-\mu)\gamma_2^4 + (3-2\mu)\gamma_2^3 + (\mu\beta - \beta - \mu)\gamma_2^2 + 2\mu\gamma_2 - \mu = 0, \tag{8}$$

$$\gamma_3^5 + (2+\mu)\gamma_3^4 + (1+2\mu)\gamma_3^3 - (1-\mu)(1-\beta)\gamma_3^2 - 2(1-\mu)(1-\beta)\gamma_3 - (1-\mu)(1-\beta) = 0, \tag{9}$$

and $SL_1 = (1-\mu-\gamma_1, 0, 0)$, $SL_2 = (1-\mu+\gamma_2, 0, 0)$ and $SL_3 = (-\mu-\gamma_3, 0, 0)$. Contrary, there is an explicit expression for the triangular points for all β:

$$SL_{4,5} = (x_{4,5}, y_{4,5}, 0) := \left(-\mu + \frac{(1-\beta)^{2/3}}{2}, \pm(1-\beta)^{1/3} \left[1 - \frac{(1-\beta)^{2/3}}{4} \right]^{1/2}, \ 0 \right). \tag{10}$$

Finally, if the sail orientation changes ($\alpha \neq 0$ or/and $\delta \neq 0$) the position of the equilibrium points are artificially displaced. For instance, if $\delta = \pm\pi/2$ and α varies, the equilibrium points are displaced to one side or the other of the Sun-sail line inside the ecliptic plane, while if $\delta = 0$ or π and α varies, the equilibrium points are displaced above or below the ecliptic plane, where all the displaced equilibria lie in a plane perpendicular to $z = 0$ containing L_i and SL_i. Finally, for any other fixed value of $\delta = \delta^*$ and varying α, the equilibrium points are displaced on an inclined plane with respect to the ecliptic containing L_i and SL_i [29, 4, 8].

3. Non-Linear dynamics around equilibria

The main goal of this paper is to find feasible transfer trajectories to the vicinity of the L_4 and L_5 points, taking advantage of the unstable invariant manifolds of the displaced SL_1 and SL_2 equilibrium points. It is true that the unstable invariant manifold structure around a displaced libration point is more complex, as it is composed of the unstable manifolds of all the periodic and quasi-periodic orbits related to the equilibrium point. Hence, one could consider any of these other unstable manifolds to find transfer orbits. However, for this preliminary work, we have only focused on the unstable manifolds related to the displaced SL_1 and SL_2 points, as this already offers a broad range of possibilities compared to the classical (no solar sail) case. As for the vicinity of L_4 and L_5, it is well-known that there exists a large Region of Practical Stability (RPS) where stationary spacecraft will remain for more that 1000 years with no need of station keeping maneuvers, which makes this location ideal for a space-weather observatory. This section analyzes the non-linear dynamics around the different SL_i equilibrium points and how these are affected by the sail parameters: β, α and δ.

3.1. SL_1 and SL_2 equilibrium points

Let us first focus on the dynamics close to the displaced collinear points SL_1 and SL_2, the equilibrium points for $\beta \neq 0$ and $\alpha = 0$ (solar sail oriented perpendicular to the Sun-sail line). Recall that as β increases these equilibrium points are shifted towards the Sun, and that the linear dynamics for SL_1 and SL_2 is always center×center×saddle. Table 2 summarizes the position and the eigenvalues of SL_1/SL_2 for $\beta = 0.01, \ldots, 0.05$. As the system is Hamiltonian for $\alpha = 0$, the two center direction give rise to two families of periodic orbits, the well-known planar and vertical Lyapunov orbits. Moreover, the coupling between the two oscillatory motion gives rise to the Lissajous and halo family of orbits. All these orbits are also known as libration point orbits (LPOs).

This paper focuses on the dynamics given by the saddle component, as it gives rise to the stable and unstable manifolds which together with the stable and unstable manifold of the LPOs configure the set of re-entry and escape trajectories related to the equilibrium point's vicinity. Note that as β increases the instability rate of SL_1 decreases while the instability rate of SL_2 increases, which has a direct effect on the escape rates from the vicinity of the equilibrium point.

The unstable manifolds of the displaced SL_1 and SL_2 equilibria are perfect candidates for providing trajectories to reach the L_4/L_5 vicinity. To illustrate this, the stable and unstable manifolds related to SL_1 and SL_2 for different values of β have been computed. This gives an idea of the general trend of the invariant manifolds and how changing the efficiency of the solar sail affects them. Figure 2 shows the stable, $W^s(SL_i)$, and unstable, $W^u(SL_i)$, manifolds for $\beta = 0$ (left), 0.01 (middle) and 0.03 (right). A general view and their relative position with respect to a subset of the RPS appears in the top plots. The bottom plots show a zoomed-in image close to the Earth. Note that all these invariant manifolds have been computed up to $t_f = 10$ years. Hence, the longer the unstable manifold path is, the faster the transfer to L_4/L_5 can be. These results are consistent with the values presented in Table 2.

Table 2: Position of the displaced equilibrium points $SL_1 = (x_{L_1}, 0, 0)$ and $SL_2 = (x_{L_2}, 0, 0)$ along the x-axis, and values of the three pair of eigenvalues $\pm\lambda$, $\pm i\omega_1$ and $\pm i\omega_2$, for $\beta = 0.01(0.01)0.05$.

β	x_{L_1}	λ	ω_1	ω_2	x_{L_2}	λ	ω_1	ω_2
0.01	0.98873101897	2.13994	1.8517	1.7749	1.00908250142	2.88718	2.3061	2.2399
0.02	0.98716671573	1.78196	1.6484	1.5679	1.00827979413	3.30472	2.5719	2.5113
0.03	0.98525423949	1.46959	1.4821	1.4010	1.00762463476	3.72982	2.8482	2.7927
0.04	0.98299017728	1.20876	1.3536	1.2762	1.00708319765	4.15761	3.1307	3.0797
0.05	0.98040996743	9.98326	1.2586	1.1886	1.00662972805	4.58492	3.4162	3.3691

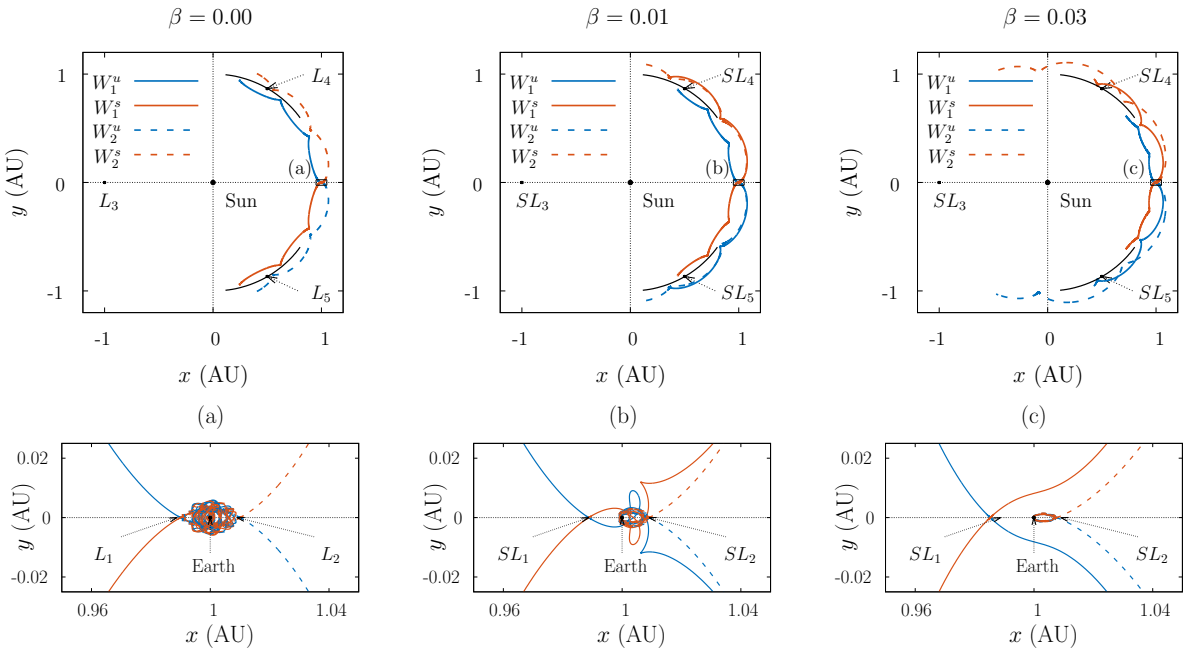

Figure 2: Stable $W_i^s = W^s(SL_i)$ (red), and unstable $W_i^u = W^u(SL_i)$ (blue) manifolds of SL_1 (solid) and SL_2 (dashed) for $\beta = 0, 0.01, 0.03$. Top: general view and relation with the region of practical stability (black). Bottom: zoom close to the Earth.

It is interesting to note that, for $\beta = 0$, the vicinity of L_4 can only be reached from L_1 and the vicinity of L_5 only from L_2. Instead, the extra acceleration produced by the solar sail ($\beta \neq 0$) allows us to reach both the vicinity of L_4 and L_5 from L_1. This is very convenient from a mission prospective. For instance, two sailcraft could be considered, one aiming for L_4 and the other for L_5, and it would allow the use of a single launch vehicle to reach the L_1 neighborhood and then inject each one to a different invariant manifold. On the other hand, from L_2 for all values of β only the L_5 vicinity can be reached, as one of the unstable invariant manifolds branches gets trapped around the Earth.

Given that solar sails are orientable surfaces, it is interesting to investigate how a change in the sail orientation can affect the trajectories starting from an initial condition along the unstable manifolds in Figure 2. Recall that, when the sail orientation is changed, the equilibrium points are displaced, as well as the location of its associated stable and unstable manifolds [9, 6]. Hence, the trajectories will escape along a new unstable direction. This can have interesting implications on the trajectories starting from initial conditions along the SL_1 and SL_2 unstable manifolds. Figure 3 shows three trajectories with different fixed values of α starting from the same initial condition $\mathbf{p}_0$ along the unstable direction ($\hat{\mathbf{v}}_1^u$) of the SL_1 equilibrium point (i.e. $\mathbf{p}_0 = SL_1 \pm h\hat{\mathbf{v}}_1^u$ and $h = 10^{-4}$). Here the sail orientation with respect to the Sun-sail

line is constant throughout the trajectory. Notice that for each of the sail orientations the final trajectories are completely different. For instance, for $\alpha = 20^\circ$ (middle) the behavior is quite similar to the one for $\alpha = 0$ (Figure 2 middle) where each leg of the unstable manifold leads to different regions of the phase space, in particular the vicinity of L_4 and L_5. On the other hand, for $\alpha = 15^\circ$ (left) the two legs of the unstable manifold move close to the Earth and then move towards the L_5 vicinity, whereas for $\alpha = -20^\circ$ (right) the two legs of the unstable manifolds are directed towards the L_4 vicinity. This illustrates the richness of the dynamics around the equilibrium points when the sail orientation changes.

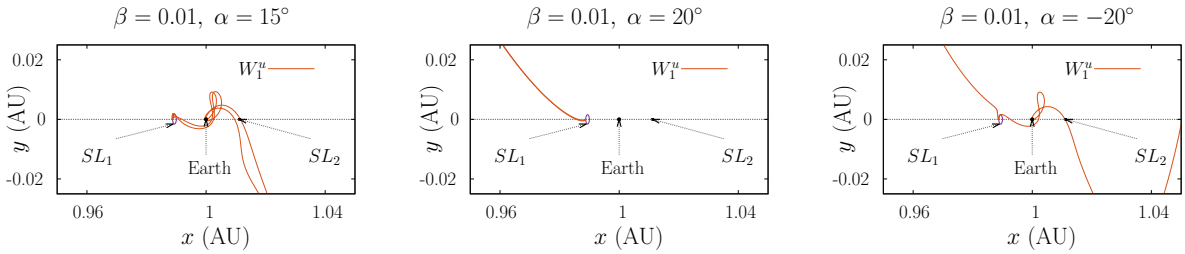

Figure 3: Propagation of initial conditions on the SL_1 unstable manifold for $\beta = 0.01$, for $\alpha = 15^\circ$ (left), $\alpha = 20^\circ$ (middle) and $\alpha = -20^\circ$ (right).

Figure 4 shows the same analysis for initial conditions $\mathbf{p}_0$ along the unstable direction ($\hat{\mathbf{v}}_2^u$) of SL_2 (i.e., $\mathbf{p}_0 = SL_2 \pm h\hat{\mathbf{v}}_2^u$ and $h = 10^{-4}$). Notice that for different values of α, the trajectories can either go towards the Earth or head towards L_5. Given that SL_2 is displaced towards the Earth as β increases, it is harder to find escape trajectories towards L_4 as one of the legs gets entangled around Earth, where the dynamics are very chaotic. This does not mean that there are no transfers from SL_2 to L_4, but that the set of sail orientations that enable such paths is small. From simulations we have observed that in most cases these natural transfers take long excursions towards L_5 before reaching the L_5 vicinity.

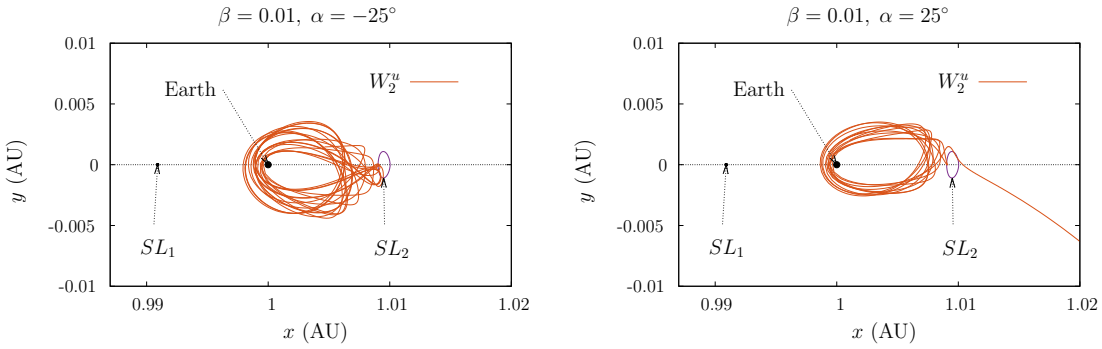

Figure 4: Propagation of initial conditions on the SL_2 unstable manifold for $\beta = 0.01$, for $\alpha = -25^\circ$ (left) and $\alpha = 25^\circ$ (right).

3.2. SL_4 and SL_5 equilibrium points

As mentioned before, the triangular Lagrangian points SL_4/SL_5 of the Sun - Earth CRTBPS are totally elliptic equilibria for all β. Under generic conditions, the KAM theorem applies around these equilibria and most of the initial conditions in a small enough neighborhood of SL_4/SL_5 lie on 3D invariant tori. Hence, a region of stability, understood in a practical sense, is expected to be found close enough to SL_4/SL_5.

Despite the fact that the available theory of Hamiltonian dynamical systems gives very valuable information about the evolution of the system around SL_4/SL_5, it is not enough when it comes to describing the shape of the full region where the invariant tori lie. Furthermore, the description of the invariant objects that conform the boundary of this region is still an open and hard mathematical problem [37]. Even with the techniques available nowadays, only brute-force explorations have been useful for giving the most basic descriptions.

In this section, these RPS around SL_4/SL_5 are studied for $\beta = 0.01, 0.02, \ldots, 0.05$ and $\alpha = 0$. An initial condition (i.e., an initial position for the solar sail) close to SL_4/SL_5 with zero synodical velocity $\dot{x} = \dot{y} = \dot{z} = 0$ is regarded as *practically stable* if the corresponding trajectory remains close to SL_4/SL_5 for a large time span. Hence, the RPS is the set of practically stable points, and can be mathematically defined as the subset of points in a box R (in appropriate coordinates) that contains SL_4/SL_5, such that the propagation forward in time of any of these points in R, initially with $\dot{x} = \dot{y} = \dot{z} = 0$, does not leave a larger set R' after a large number of years $T \gg 0$. Figure 5 shows the choice of R and R' in the CRTBPS around L_4. The boundary of R' defines the *escaping criterion*: if a trajectory crosses this boundary at some time, the initial point is considered not to belong to the RPS. Note that, since we are assuming that the trajectories start with zero synodical velocity, the RPS is a 3D set. However, in this paper only the RPS in the ecliptic plane is considered, i.e., $z = 0$.

The triangular points SL_4/SL_5 have zero synodical velocity and the RPS is understood as a set of initial conditions that remain close to these points for a sufficiently long time span. For this reason the initial conditions in the RPS are chosen to satisfy $\dot{x} = \dot{y} = \dot{z} = 0$. One expects that, for small enough initial synodical velocity, one would also find an analogous RPS, but certainly smaller; and the size and shape of such an analogous region should be studied on a case by case basis. Depicting and studying the region as done provides a global picture of up to which extent there are orbits that oscillate around the triangular points. Moreover, this paper focuses on justifying that transfers to the triangular points are, in fact, feasible, but for concrete applications one would target a specific invariant object, e.g. a periodic orbit inside the RPS.

To study the RPS, one relies on simulations, and for that one has to fix a maximal number of years T. The shape and size of the detected RPS depends strongly on the choice of T. Since we systematically deal with numerical approximations with some fixed resolution, one expects to be able to find, for each choice of the systems parameters, a value $T = T_{\max}$ such that the differences with the detected RPS for $T_{\max}$ and any $T > T_{\max}$ is negligible. For the sets of parameters studied here, we have propagated up to $T_{\max} = 10^4$ years. Recall that a generic trajectory close to a totally elliptic equilibrium point of a Hamiltonian system with three or more degrees of freedom will eventually escape due to the so-called Arnold diffusion, but that this would take exponentially long times. This concerns the mathematical problem within, but for mission applications, a study with $T = 10^3$ years suffices.

3.2.1. Approximation of the RPS

Due to the symmetries of the system, it is sufficient to study the RPS around one of the two triangular equilibria, so in what follows the analyses are restricted to the dynamics around SL_4. The most efficient way to approximate the RPS is by using a brute-force exploration of the region close to SL_4 for some value of $T = T_0$, and then perform a sequence of refinements for larger values of $T > T_0$ by only checking the boundary of the first approximation. Due to the shape of this region in x, y coordinates (see Figure 6 left), it is convenient to consider polar coordinates $(r, \theta) \in (-(1-\beta)^{1/3}, \infty) \times [-0.5, 0.5)$ (measured in AU and rad$/(2\pi)$, respectively) whose origin of coordinates corresponds to the position of SL_4:

$$x = \mu + (r + r_4)\cos(2\pi\theta + \theta_4), \quad y = (r + r_4)\sin(2\pi\theta + \theta_4), \quad z = 0, \tag{11}$$

where $r_4 = \sqrt{(x_4 + \mu)^2 + y_4^2}$ and $\theta_4 = \arctan(y_4/(x_4 + \mu))$ are the polar coordinates of SL_4 (see Eq. 10). Note that positive angles are counted counterclockwise. As a result, the points in the RPS closest to the Earth correspond to the smallest (negative) values of θ.

Below, the method used to approximate the RPS is described (we refer to Refs. [37, 10] for a more detailed exposition).

Step 1: First approximation. Fix $T = T_0$ and an equidistant grid of points in some adequate box R in (r, θ). Each point in the grid defines an initial condition $(x(r,\theta), y(r,\theta), 0, 0, 0, 0)$ according to Eq. 11, and these are integrated for $T = T_0$ years. The *escaping criterion* here is to cross the hypersurface $y = -0.5$ or to collide with one of the two primaries [12]. So, if for some $t < 2\pi T_0$ it happens that $y < -0.5$ or $r_{ps} < 10^{-4}$ or $r_{pe} < 10^{-4}$, the initial condition is considered not to belong to the RPS. Otherwise, if the trajectory is integrated until $t = 2\pi T_0$ without this happening, we consider that the initial condition belongs to the RPS.

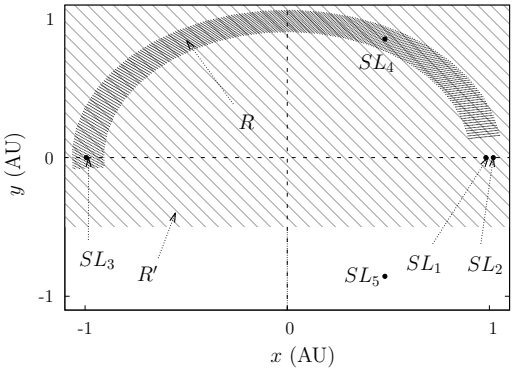

Figure 5: Schematic view of the regions R and R' related to the CRTBP phase space. Here $R = [-0.08, 0.08] \times [-0.15, 0.35]$ in polar coordinates (r, θ) (Eq. 11) and R': $y \geq -0.5$ is the region in which the trajectory has to remain for T years for it to be considered as stable in a practical sense.

Step 2: Successive refinements. The first refinement consists of considering $T_1 > T_0$ and of integrating again the points in the grid that are boundary points. Boundary points are points that belong to the RPS for $T = T_0$ such that at least one of its adjacent neighbors escaped. These points are classified according to the same escaping criterion but now with T_1 instead of T_0: if for some $t < 2\pi T_1$ it happens that $y < -0.5$ or collides with one of the two primaries, it is considered an escaping point and non-escaping otherwise. Note that every time a boundary point escapes for T_1 the shape of the boundary changes and more boundary points are generated, so this process has to be repeated until none of the points on the boundary escapes in at least T_1 years.

This process can be repeated for a sequence of increasing values of T, $T_2 < T_3 < \cdots < T_n$ until the desired $T_{\max}$ is reached.

This method substantially reduces the computational cost to determine the RPS, since it avoids reiterating points closer to SL_4, where one expects exponentially long escape times, and only the fastest escaping initial conditions are studied.

3.2.2. A common target region for $\beta \leq 0.05$

For realistic values of β one does not expect the shape and size of the RPS to differ much from the non-sail case $\beta = 0$. Therefore, this section studies the evolution of the RPS as β increases. To do so, a 1000×1000 grid in $(r, \theta) \in R = [-0.0008, 0.0008] \times [-0.35, 0.15]$ is considered, for the values of $\beta = 0.01, \ldots, 0.05$. Figure 5 shows a depiction of R that is 100 times wider. It is worth noting that for all the cases that have been considered $T_{\max} = 10^4$ years[3]. For smaller values of $T_{\max}$ the region appears to be much larger and present a less defined boundary. Figure 6 shows the RPS for $\beta = 0.01$ and $\beta = 0.05$. In the left plot, the RPSs are displayed in actual x, y synodic coordinates. If compared to Figure 5, one can see that the RPSs are contained in a set as the one displayed in the region labeled as R in the sketch. In the right plot a

[3]The computation for each value of β takes approximately 20h of CPU time.

detailed view of these two cases in (r, θ) coordinates is shown. Again, comparing with the sketch of Figure 5, this right plot shows the shape of the RPS in R, choosing adequate coordinates in it (say, straightening the region out). In this right plot, the fact that these are centered in SL_4 allows for comparison of the regions for different values of β between each other.

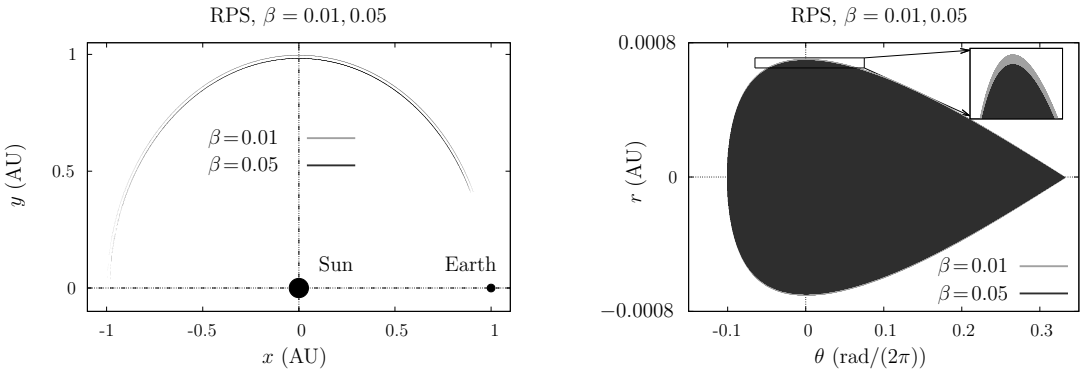

Figure 6: RPS around SL_4 for $\beta = 0.01$ and $\beta = 0.05$. Left: Original coordinates (x, y). Right: Detail in (r, θ) coordinates.

A global picture of the obtained results can be described as follows: in all the studied cases, it can be observed that the RPS is extremely narrow in r compared to θ. More concretely, the regions have approximately a width of 0.0016 AU and a length of π AU, a difference of 3 orders of magnitude. Also, the region moves towards the position of the Sun as β increases, as does the SL_4 point (see Eq. 10). Moreover, for the studied values of β, the area of the RPS seems to decrease as β increases as it can be seen on the detail in the right plot in Figure 6. Namely for $\beta = 0.01$ the area of the RPS is of the order of 4×10^{-4} AU^2, or 8.97×10^{12} km^2, while for $\beta = 0.05$ this area has decreased to 3.95×10^{-4} AU^2, or 8.83×10^{12} km^2. The behavior of the area of the RPS as a function of β is studied in [10].

Despite the fact that the area of the RPS decreases as β increases, the size and shape of the regions for the considered values of β is very similar. Hence one can define a prospective target region (that is a subset of the full RPS) for trajectory design around the SL_4 point, that is the same for all studied values of β.

According to KAM and Nekhorosev theories, the RPS around SL_4/SL_5 exist due to the presence of nested 3D invariant tori that collapse at these two equilibria. The trajectory of an orbit on one of these 3D tori, or very close to it, will be seen as oscillating in the x, y projection. The amplitude of these oscillations will tend to 0 as the chosen torus is closer to SL_4/SL_5. If a trajectory is designed to arrive to the boundary of the RPS, that trajectory would oscillate along the whole RPS, experiencing excursions in x and y coordinates with an amplitude of order up to 2 AU and 1 AU, respectively. Hence, the common target region should be chosen so that these oscillations have smaller amplitudes, or equivalently, that they remain closer to the triangular points along the orbit.

These oscillatory motions are measured by keeping track of how much the coordinates (r, θ) vary along the trajectories starting from initial conditions inside the RPS. So, during the course of the integration, the maximal (M) and minimal (m) values of r and θ attained during the orbit have been computed, and are denoted as $r_{\rm M}$, $r_{\rm m}$, $\theta_{\rm M}$ and $\theta_{\rm m}$. The observables to take into account are

$$\Delta r = r_{\rm M} - r_{\rm m}, \qquad \Delta\theta = \theta_{\rm M} - \theta_{\rm m}.$$

For all the studied values of $\beta \in [0, 0.05]$, and all initial conditions that belong to the RPS, it has been observed that $\Delta r \in [0, 0.01]$ AU and $\Delta\theta \in [0, 0.45]$ rad/(2π). As expected, the initial conditions with smaller Δr and $\Delta\theta$ are those closer to $r = 0$ and $\theta = 0$, i.e., closer to SL_4, while the outermost points of the RPS are those that experience wider oscillations: during the propagation of the initial conditions in the RPS, the r coordinate can move over 10^7 km and the θ coordinate spans the first two quadrants in the x, y plane.

Figure 7 shows how the amplitude oscillations vary. Each of the six regions in the plots correspond to initial conditions whose trajectories oscillate in Δr (right) and $\Delta\theta$ (left) within some interval. These

intervals have been labeled from 1 to 6 and group a range of oscillations: $\Delta r_i \in [0.0017 \cdot (i-1), 0.0017 \cdot i)$ and $\Delta\theta_i \in [0.075 \cdot (i-1), 0.075 \cdot i)$.

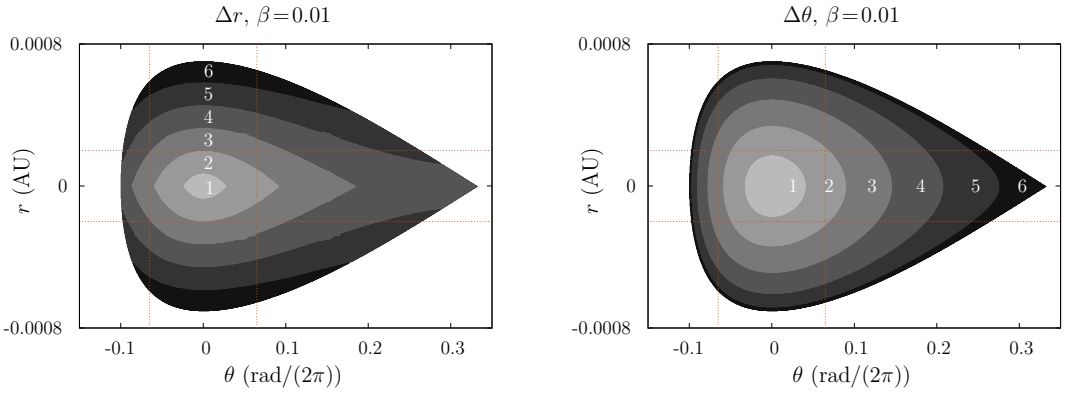

Figure 7: Maximum oscillations in Δr (left) and $\Delta\theta$ (right) of orbits starting at the RPS for $\beta = 0.01$ and integrated over $T = 10^3$ years. Each shade of gray indicates an interval of oscillations: $\Delta r \in [0.0017 \cdot (i-1), 0.0017 \cdot i)$ and $\Delta\theta \in [0.075 \cdot (i-1), 0.075 \cdot i)$ for $i = 1, \ldots, 6$. The vertical (resp. horizontal) red dotted lines correspond to $\theta = \pm 0.065$ (resp. $r = \pm 0.0002$).

Regions where the probe's trajectory oscillates in a controlled manner are of interest for mission applications. Hence, for the optimization problem in the forthcoming sections, the set of target points that has been chosen to exemplify is a region that in the left and right plots of Figure 7 is close to SL_4: approximately the region labeled with a 2. Other target region could be considered depending on the mission requirements, and the analysis in the forthcoming sections would apply analogously. As will be seen, if the targeted region is closer to SL_4 the time required to reach this region will be larger. Analogously, for wider target regions the time to reach the region decreases. These orbits experiment oscillations of at most $\Delta r < 0.034$ AU and $\Delta\theta < 0.15$ rad/(2π) for integrations up to $T = 1000$ years. A good approximation of this region is the interior of the ellipse:

$$\mathcal{R}: \quad \left\{ (r,\theta) \in \mathbb{R}^2 \quad | \quad \left(\frac{r}{r_{\max}}\right)^2 + \left(\frac{\theta}{\theta_{\max}}\right)^2 \leq 1 \right\}, \tag{12}$$

where $r_{\max} = 0.0002$ and $\theta_{\max} = 0.065$. Despite being a relatively elongated set of target orbits, the optimization problem for a smaller set by reducing the value of $\theta_{\max}$ will also be studied at the end of Section 4.4.2.

Finally, to illustrate the behavior of these orbits inside the RPS, two orbits within region $\mathcal{R}$ for $\beta = 0.01$ have been propagated. One starting at $(r_0, \theta_0) = (0, 0.0325)$ and another one starting at $(r_0, \theta_0) = (0.0001, 0)$. These correspond to the left and right plots in Figure 8. Note that to be able to see oscillations, the integration has been performed up to $T = 500$ years. Since the width of the region in (x, y) coordinates is very narrow, it is convenient to use again the (r, θ) coordinates to visualize the motion of the probe.

Both plots of Figure 8 show some regularity in the motion. It is plausible to think that these orbits are close to a 3D KAM invariant torus. Qualitatively, these orbits display distinctive features. On the left plot, the projection in the (r, θ) plane of orbit starting at $r = 0$ oscillates both in r and θ with seemingly constant amplitudes. While on the right, for $r \neq 0$ the amplitude of the oscillations in r change much more along the propagation. These oscillations depend on how close to which 3D KAM torus the orbit evolves, a problem which requires further investigations and is left for future contributions.

4. Transfer to SL_4 and SL_5 RPS

As previously mentioned, in this paper, we propose to use the displaced L_1 and L_2 points as gate-ways for transfers towards the target subset $\mathcal{R}$ in the RPS at SL_4/SL_5. To obtain time-optimal transfers a two-step

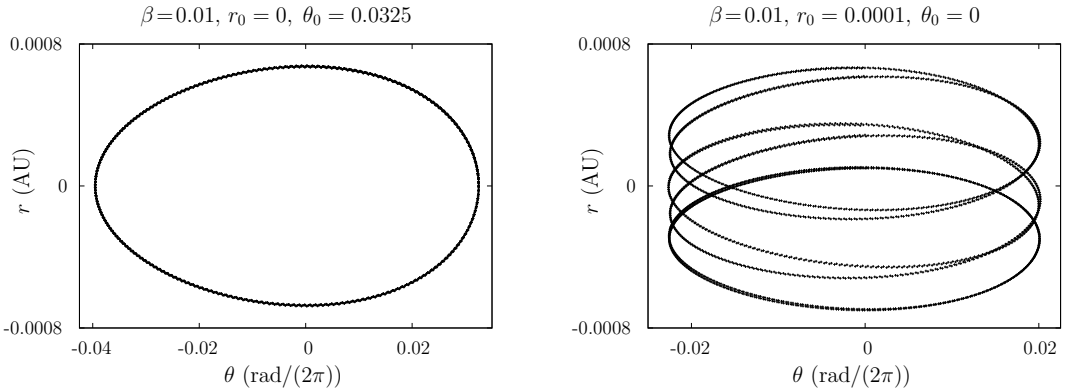

Figure 8: Examples of orbits inside the RPS for $\beta = 0.01$. Left: $(r_0, \theta_0) = (0, 0.0325)$. Right: $(r_0, \theta_0) = (0.0001, 0)$.

process has been performed. First, transfer trajectories taking advantage of the unstable manifolds related to the displaced L_1 and L_2 are generated. These candidates trajectories are constructed as a concatenation of piece-wise arcs, where the sail orientation is kept constant throughout each of the arcs. Second, these solutions are used as an initial guess to find time-optimal transfer trajectories between the displaced L_1/L_2 points and the subset $\mathcal{R}$ of the SL_4/SL_5 RPS.

4.1. Finding an initial guess

A simple transfer strategy to reach $\mathcal{R} \subset$ RPS at $SL_{4,5}$ is proposed, which only requires three maneuvers: (1) set $\alpha = \alpha_0$ and travel along the unstable manifold related to an equilibrium point from the SL_1/SL_2 families; (2) when a given Poincaré section Σ_1 is reached, the sail orientation is set to $\alpha = \alpha_1$ to insert the solar sail on a transfer trajectory that reaches the target region $\mathcal{R}$ around $SL_{4,5}$; and (3) once the sail reaches $\mathcal{R}$ the sail is set perpendicular to the Sun-sail line ($\alpha = 0°$) to remain there. The Poincaré section used is $\Sigma_1 = \{y = \pm(x - \mu)/\sqrt{3}\}$, a hyper-plane at the mid-distance between the Sun - Earth line and the $SL_{4,5}$-Sun line. Note that this particular hyper-plane cuts through the xy plane $\pm 30°$ from the xz plane; a hyper-plane that is at the same distance from $L_{1,2}$ as from $L_{4,5}$. Other Poincaré sections could be considered but from previous explorations [6] this section provides the largest amount of possible transfer trajectories. Figure 9 shows a schematic representation of this three-step strategy.

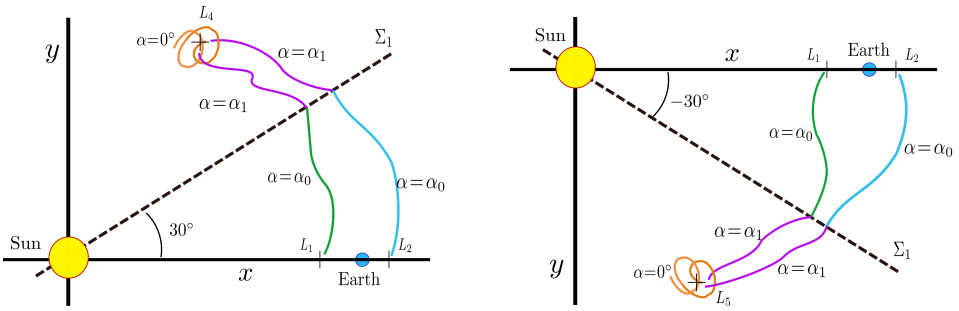

Figure 9: Schematic representation of a three-step transfer strategy from the SL_1, SL_2 vicinity to a subset of the SL_4 (left) and SL_5 (right) regions of practical stability.

To generate these transfer trajectories, a brute-force search has been performed. For a fixed β, different initial conditions ($\mathbf{x}_0$) are taken along the two directions of the unstable vector ($\hat{\mathbf{v}}^u_{1,2}$) related to SL_1 and SL_2 respectively (i.e., $\mathbf{x}_0 = SL_{1,2} \pm h\hat{\mathbf{v}}^u_{1,2}$ and $h = 10^{-5}, 5 \times 10^{-5}, 10^{-4}$). For each initial condition ($\mathbf{x_0}$) a

set of different fixed sail pitch angles $\alpha_i \in [-65°, 65°]$ is considered, and integrated (forward in time) until the trajectory reaches Σ_1. Additionally, a grid of initial conditions belonging to the subset $\mathcal{R}$ of the $SL_{4,5}$ RPS are taken (i.e., $x = (r + r_{4,5})\cos(2\pi\theta + \theta_{4,5}) - \mu$, $y = (r + r_{4,5})\sin(2\pi\theta + \theta_{4,5})$, $z = \dot{x} = \dot{y} = \dot{z} = 0$ where (r, θ) satisfy $(\frac{r}{r_{\max}})^2 + (\frac{\theta}{\theta_{\max}})^2 \leq 1$ with $r_{\max} = 0.0002$ and $\theta_{\max} = 0.065$). Again for each point in the region the trajectory is integrated (backwards in time) for different fixed sail orientations ($\alpha_j \in [-65°, 65°]$) until the trajectory reaches Σ_1. In both cases, if the trajectory comes too close to Earth ($r_{pe} < 10^{-4}$ AU) or takes more than 10 years to reach Σ_1 the integration is stopped and the trajectory discarded.

Finally, a comparison between the two sets of points, the ones arriving from $SL_{1,2}$ with those arriving from $SL_{4,5}$ on the section Σ_1, is performed in order to determine intersections (or quasi-intersections) in position and velocity. A first filtering process has been performed where all trajectories whose difference in position at Σ_1 is larger than 5×10^{-4} AU and that require a sail orientation change ($\Delta\alpha$) larger than 60° at Σ_1 have been discarded. All the resulting trajectories, although they have a discontinuity at Σ_1, are candidate trajectories to be refined with a shooting method, or can be used as an initial guess for an optimization problem. Other values for the errors in position and orientation change at Σ_1 could be considered for the filtering process, resulting in a different set of candidate trajectories for the optimization process. The instant attitude change at the section will be smoothened out by the optimizer in the next step, where large sudden changes are not recommended.

The brute-force search process described above has been performed for $\beta = 0.01$ and transfer trajectories from: (a) SL_1 to SL_4, (b) SL_1 to SL_5, (c) SL_2 to SL_4 and (d) SL_2 to SL_5. Table 3 summarizes for each of the four types of transfers analyzed: the required change in the sail orientation $\Delta\alpha$ at Σ_1; the transfer time to reach $\mathcal{R}$; and the difference in velocity Δv at Σ_1. Notice that there is a larger set of possible transfer trajectories from SL_1 to both SL_4 and SL_5, than there is when starting from SL_2. Furthermore, the solutions starting at SL_1 show a larger range of transfer times and Δv-values at the section.

Table 3: Filtered initial guess results

	# filtered	$\Delta\alpha$ (min-max)	Estimated transfer times	Estimated Δv at Σ_1
SL_1 to SL_4	15774	$20° - 60°$	ranges from 681 to 1530 days	from 270 to 600 m/s
SL_1 to SL_5	1557	$20° - 55°$	ranges from 1250 to 4000 days	from 500 to 150 m/s
SL_2 to SL_4	93	$20° - 45°$	$\approx$ 3568 days	$\approx$ 500 m/s
SL_2 to SL_5	1414	$35° - 50°$	$\approx$ 988 days	$\approx$ 600 m/s

From all the trajectories in Table 3 and each of the $SL_{1,2}$ to $SL_{4,5}$ sequences, two candidate trajectories have been selected as initial guesses for solving the time-optimal problem: one which presents the smallest transfer time and one with the smallest discontinuity in velocities at Σ_1. Figure 10 shows the candidate transfer trajectories with minimum transfer time from the SL_1 unstable manifold to SL_4 (green) and SL_5 (purple). Looking at the behavior of these trajectories close to Earth (Figure 10 right) notice how the transfer trajectory towards SL_5 performs a fly-by close to Earth to reach the vicinity of SL_2 before it starts the excursion towards SL_5. This explains the difference in transfer times seen in Table 3 where the transfer trajectories from SL_1 to SL_4 take between 681 to 1530 days and the transfers from SL_1 to SL_5 take between 1298 to 4000 days. Figure 11 shows the minimum transfer time candidate starting from the SL_2 unstable manifold to SL_4 (green) and SL_5 (purple). Notice that here the transfer trajectory toward SL_4 performs a long excursion passing close to SL_5. This is due to how the trajectories have been constructed and due to the fact that the first leg from the unstable manifolds around SL_2 either goes towards the Earth or moves towards SL_5. This large excursion explains the long transfer times seen in Table 3, where the transfer to SL_4 takes 3 times longer than the transfer time to SL_5.

4.2. Optimized solutions

While the results of Section 4.1 provide valuable insights in the capability of solar sails to transfer between the displaced L_1 and L_2 points and the region $\mathcal{R}$ at L_4/L_5, the trajectories obtained are sub-optimal from a transfer time perspective. In addition, the small discontinuity in the state vector at the Poincaré section renders the trajectories unfeasible in practice. However, these solutions do provide an excellent initial guess

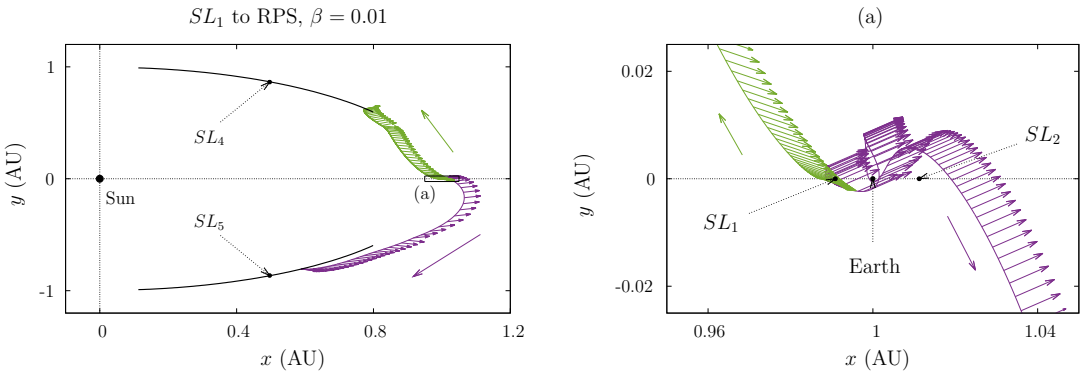

Figure 10: Selected initial guess transfer trajectories from the SL_1 unstable manifold to the RPS around SL_4 (green) and SL_5 (purple). Left: full trajectories, Right: zoom close to Earth.

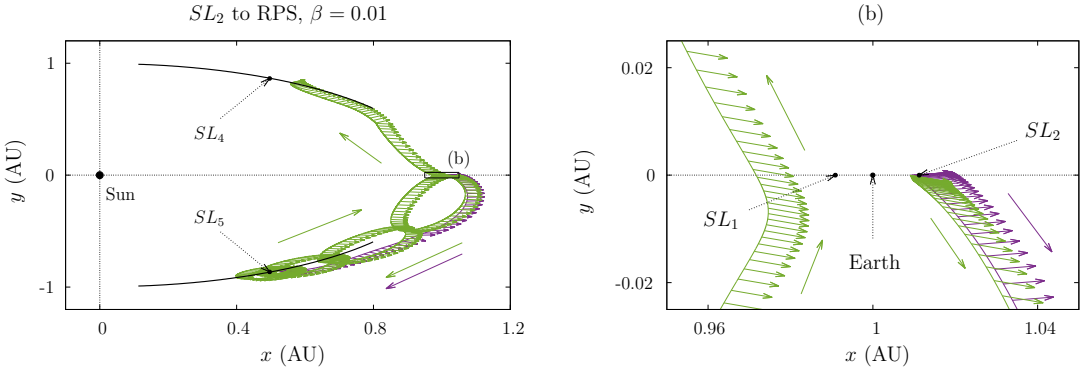

Figure 11: Selected initial guess transfer trajectories from the SL_2 unstable manifold to the RPS around SL_4 (green) and SL_5 (purple). Left: full trajectories, Right: zoom close to Earth.

to find time-optimal transfers between the SL_1/SL_2 points and the SL_4/SL_5 stability regions. Therefore, the accompanying optimal control problem needs to be defined and solved.

The goal is to find the time history of the states of the sailcraft, $\mathbf{x}(t) = (x, y, \dot{x}, \dot{y})$, and its control, $u(t) = \alpha$, that minimize the transfer time from SL_1/SL_2 to the subset $\mathcal{R}$ of the RPS around the triangular points. Therefore, the objective is defined as:

$$J = t_f - t_0, \tag{13}$$

where t_f and t_0 are the final and initial time of the trajectory. The dynamics to be satisfied are given by Eq. 1 restricting the motion to the ecliptic plane ($z = \dot{z} = 0$). The start of the transfer needs to coincide with the displaced L_1 or L_2 points whose state vectors are given by $\mathbf{x}_{SL} = (x_{SL}, 0, 0, 0)$. The values for x_{SL} for a range of solar sail lightness numbers are given in Table 2. Hence, the boundary condition on the initial state vector is defined as:

$$\mathbf{x}_0 = \mathbf{x}(t_0) = \mathbf{x}_{SL}. \tag{14}$$

Furthermore, the end point of the trajectory needs to coincide with the region $\mathcal{R}$ at SL_4 or SL_5, and the sailcraft needs to arrive at that point with zero synodical velocity. To allow the optimizer to select the best arrival location within $\mathcal{R}$, two static parameters have been defined, $\mathbf{k} = (r, \theta)$, where r and θ represent the polar coordinates of the arrival location around the triangular Lagrange point as described in Section 3.2. In order for these polar coordinates to lie within $\mathcal{R}$ the following constraints are applied. The first (and

equal to Eq. 12) is:

$$\left(\frac{r}{r_{\max}}\right)^2 + \left(\frac{\theta}{\theta_{\max}}\right)^2 \leq 1, \tag{15}$$

with $r_{\max} = 0.0002$ and $\theta_{\max} = 0.065$. Then, to ensure that the final state vector matches this arrival location, the polar coordinates r and θ are transformed into Cartesian position coordinates, (x_R, y_R) using Eq. 11. This enables the definition of the following additional constraint on the final state vector:

$$\mathbf{x}_f = \mathbf{x}(t_f) = (x_R, y_R, 0, 0). \tag{16}$$

Equations 14 to 16 define the set of event constraints.

Finally, the bounds on the states, control and parameters need to be defined. Note that the bounds on the states are case-specific. For example, for the transfer from SL_1 to SL_5 we defined them as:

$$(0, -1, -0.25, -0.25) \leq \mathbf{x}(t) \leq (1.2, 0.1, 0.25, 0.25). \tag{17}$$

The bounds on the control (i.e., on the pitch angle) are given as constraints on the sail orientation (Eq. 3):

$$-\pi/2 \leq u(t) \leq \pi/2 \tag{18}$$

Notice that no limitations on the steering capabilities are introduced, but these may be considered in future studies. Finally, the bounds on the parameters are:

$$(-r_{\max}, -\theta_{\max}) \leq \mathbf{k} \leq (r_{\max}, \theta_{\max}). \tag{19}$$

In this paper, the optimal control problem defined in Eqs. 13 - 19 is solved by using PSOPT[1], which is a particular implementation of a direct pseudospectral method in C^{++}. This method discretizes the states, $\mathbf{x}(t)$, and controls, $u(t)$, at a predefined number of nodes and uses Legendre polynomials to approximate and interpolate the dependent variables at those nodes. To solve the resulting non-linear programming problem, PSOPT is interfaced to IPOPT (Interior Point OPTimizer) [43], an open source C++ implementation of an interior point method for large scale problems. PSOPT includes options for mesh refinements and automatic scaling through the ADOL-C (Automatic Differentiation by OverLoading in C++) [15] library for the automatic differentiation of the objective, dynamics and constraint functions. In order to initialize the optimization, PSOPT requires an initial guess, for which the minimum-time trajectories from Section 4.1 are employed.

Results have been obtained for the same sets of transfers studied in Section 4.1: from SL_1 to the region $\mathcal{R}$ at SL_4 and SL_5 and similarly from SL_2. Let us first analyze the results for a transfer from SL_1 to SL_4 and $\beta = 0.01$ which appear in Figure 12. The transfer itself is shown in the top-left plot with a zoomed view of the initial and final conditions in the top-right plot. These figures show that the optimizer converges to a solution that targets the outer edge of the stability region closest to Earth where $\mathbf{k} = (0, 0.065)$. This shortens the distance to be traveled and therefore minimizes the time of flight to 669 days, reducing the time of flight compared to the solution in Section 4.1 by 12 days or 1.7%. Details on the control profile are provided in the two bottom plots of Figure 12, which show the solar sail normal vector and solar sail pitch angle, respectively. Both plots show a relatively smooth control profile, though requiring rapid changes to orientations where the sail is "switched off", i.e., when $\alpha = 90$ deg. As already mentioned, future investigations will explore options to constrain the solar sail steering capabilities, e.g., similar to the work by Heiligers et al. [20]. Such limitations will come at a cost in terms of an increase in the time of flight.

Using the result from Figure 12 as an initial guess, a continuation on the value for β can be initiated to obtain results for lightness numbers larger than $\beta = 0.01$. Note that a change in β requires a change in the location of the displaced Lagrange points and therefore a change in the boundary conditions given by Eq. 14 and Eq. 16. The transfer times for each of the transfers are summarized in the first row of Table 4. The top plots of Figure 13 furthermore show the transfer trajectories from SL_1 to SL_4. The zoomed image on the right hand-side shows the shift in both SL_1 and the region $\mathcal{R}$ around SL_4 as a function of β. The trend in the transfer time and a function of β is plotted in Figure 14 as a solid blue line. There it can seen

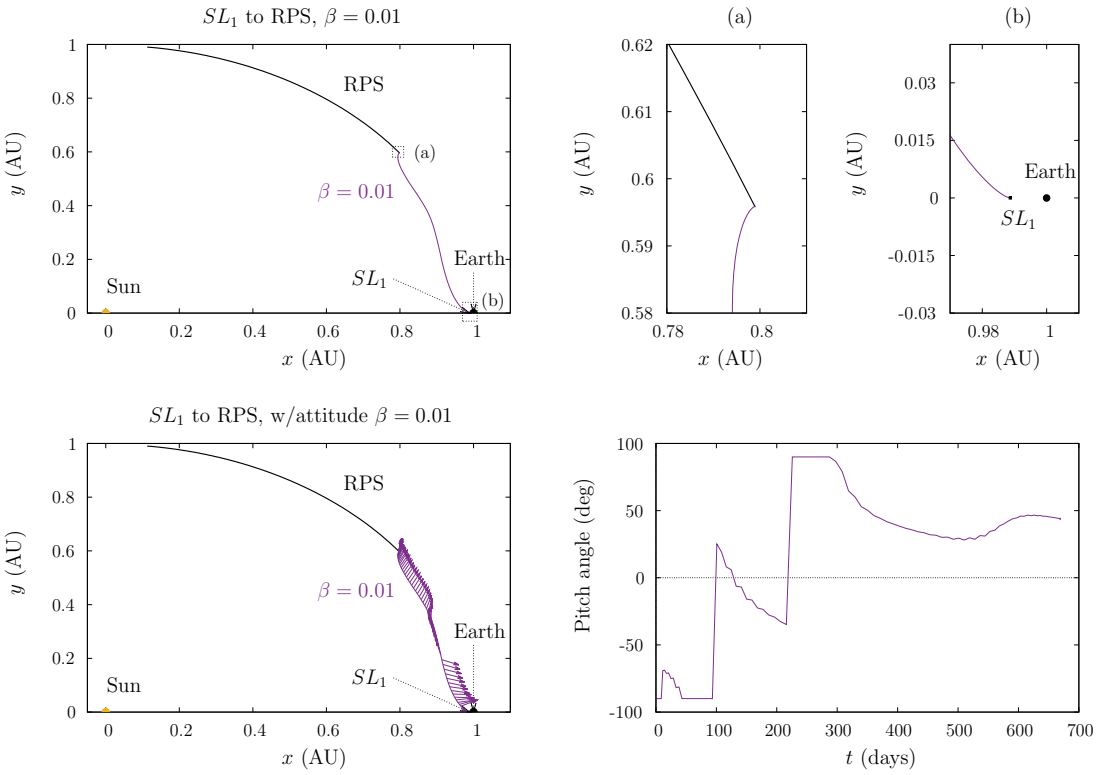

Figure 12: Top left: time-optimal transfer trajectory from SL_1 to $\mathcal{R}$ at SL_4. Top right: details of initial and final conditions. Bottom left: transfer trajectory including solar sail normal vector. Bottom right: control profile $u(t)$.

that by increasing the lightness number to $\beta = 0.05$, the transfer time can be reduced to 320 days, which is less than half the transfer time for $\beta = 0.01$ (see also Table 4).

A similar analysis has been conducted for the transfers from SL_1 to SL_5 and from SL_2 to SL_4/SL_5, which can be seen in the bottom row of Figure 13 and Figure 15, respectively. The corresponding times of flight are summarized in Table 4 and Figure 14. Comparing the transfer from SL_1 to SL_4 with the one from SL_1 to SL_5 shows a significantly longer time of flight for the latter as the optimizer only finds feasible trajectories that pass by the L_2 point. A similar comparison and conclusion can be drawn for the transfer from SL_2 to SL_4 that can only be achieved by passing by the L_1 point. The significant reduction in time of flight between the initial guess and $\beta = 0.01$ for the SL_1 to SL_5 transfer is mainly due to the fact that the optimizer targets the edge of the stability region, while the initial guess enters the stability region much closer to the SL_5 point. Furthermore, for the SL_2 to SL_4 transfer, the improvement is due to the fact that the optimized transfer no longer has to pass by the L_5 point (see Figure 11 left) and can instead directly connect the SL_2 and SL_4 points. Finally, the results for varying values of the lightness number in Figure 14 show similar reductions in times of flight between $\beta = 0.01$ and $\beta = 0.05$ as for the transfer from SL_1 to SL_4: between 44.4% and 67.2%.

A final analysis has been carried out for the time-optimal transfers from SL_1/SL_2 to SL_4/SL_5, considering the effect of reducing the size of $\mathcal{R}$. This size can be varied by changing the bounds on the parameter $\theta_{\max}$, see Eq. 19. Results are created using a continuation method where now the lightness number is kept fixed and the value of $\theta_{\max}$ is slowly reduced. Figure 16 shows the results for $\beta = 0.01$ and $\theta_{\max} = [0.065, 0.06, 0.055, \ldots 0.005]$ for the transfer from SL_1 to $\mathcal{R}$ at SL_4. Notice that, the smaller the value of $\theta_{\max}$, the smaller the stability region is. The RPS for the smallest value for $\theta_{\max}$ ($\theta_{\max} = 0.005$) is shown in the right plot of Figure 16. Through the continuation, the optimizer can easily adapt to the change in stability

Table 4: Transfer times for the initial guess and optimized solutions.

	Initial guess $\beta = 0.01$	Optimized $\beta = 0.01$	Optimized $\beta = 0.02$	Optimized $\beta = 0.03$	Optimized $\beta = 0.04$	Optimized $\beta = 0.05$
SL_1 - SL_4	681	669	458	386	345	320
SL_1 - SL_5	1298	986	703	602	563	538
SL_2 - SL_4	3568	1430	843	630	532	469
SL_2 - SL_5	988	888	645	564	522	494

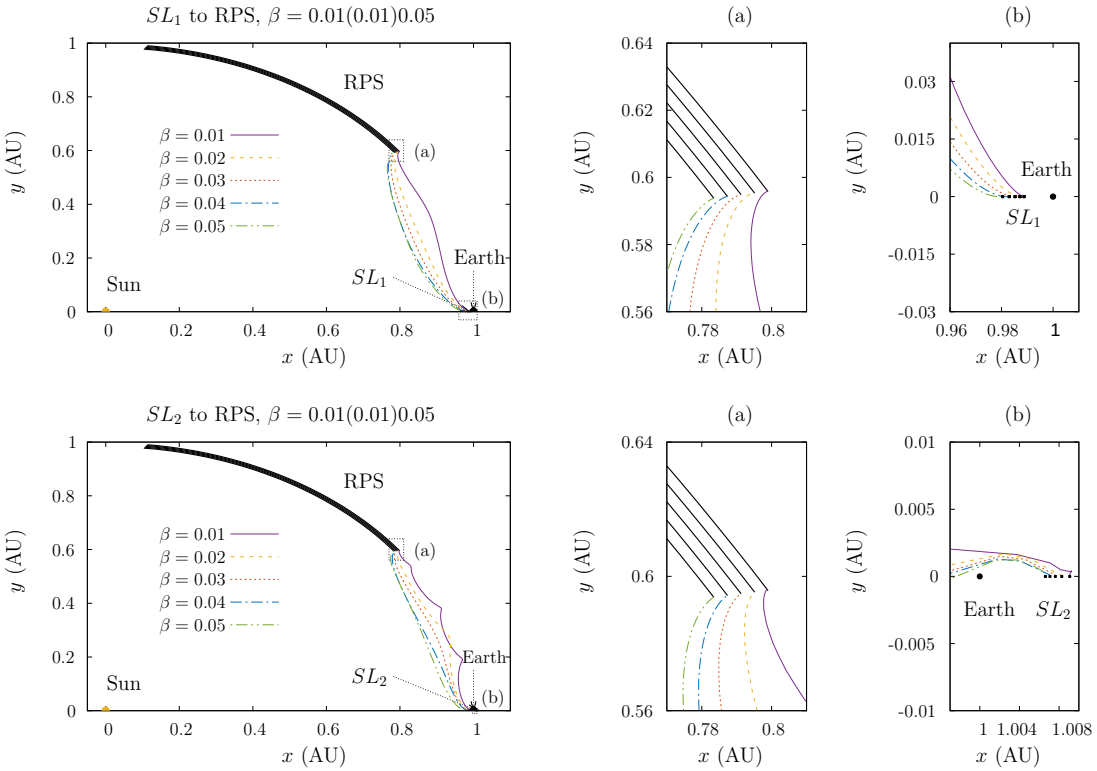

Figure 13: Time-optimal transfers from SL_1/SL_2 to $\mathcal{R}$ at SL_4. Plots on the right are close-ups of the trajectories on the left. Top row: SL_1 to SL_4 transfer, Bottom row: SL_2 to SL_4 transfer.

region size and always converges to a solution where the transfer enters the region of practical stability at the point closest to Earth, which is clearly demonstrated in the right plot of Figure 16. The effect on the time of flight appears in the left plot in Figure 14, which shows an approximately linear relation between the time of flight and $\theta_{\max}$. For $\theta_{\max} = 0.005$ the transfer time is increased to 806 days compared to 669 days for the nominal value of $\theta_{\max} = 0.065$.

5. Conclusions

In this paper the use of solar sails to enable transfer trajectories from the displaced L_1/L_2 equilibrium points to the RPS that appears in the vicinity of L_4/L_5 has been analyzed. A preliminary analysis has been performed studying the dynamical implications of these regions due to changes in the solar sail parameters. This knowledge has then been used to find simple piece-wise trajectories that transfer from one region to the other. Finally, time-optimal transfers have been obtained by means of a pseudospectral optimization method using these piece-wise simple trajectories as initial guesses.

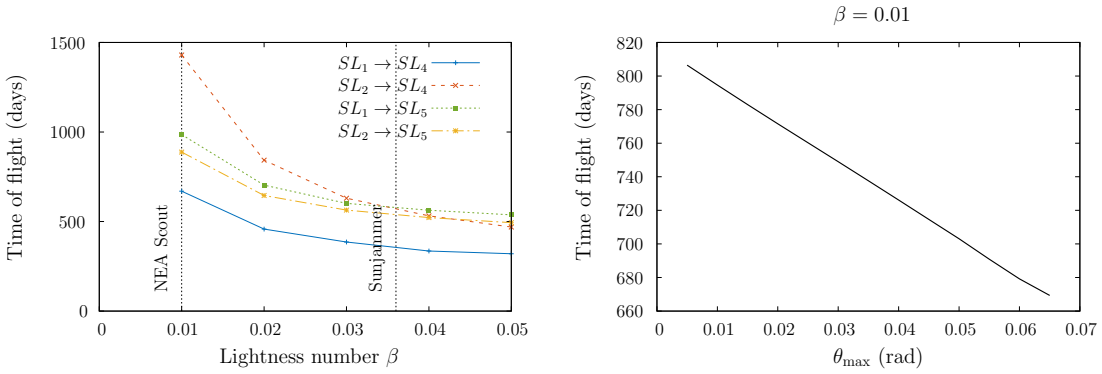

Figure 14: Left: Optimal transfer time from SL_1/SL_2 to $\mathcal{R}$ at SL_4/SL_5 as a function of the solar sail lightness number. Right: Optimal transfer time for $\beta = 0.01$ as a function of $\theta_{\max}$ for SL_1 to $\mathcal{R}$ at SL_4.

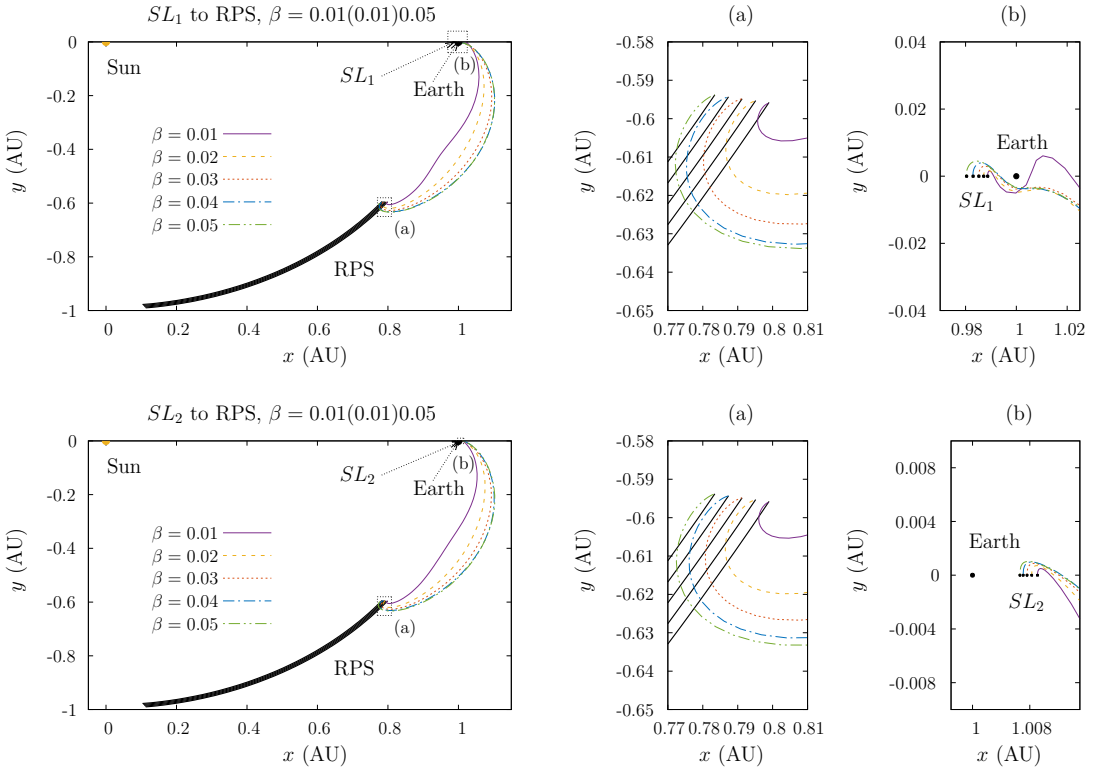

Figure 15: Time-optimal transfers from SL_1/SL_2 to $\mathcal{R}$ at SL_5. Plots on the right are close-ups of the trajectories on the left. Top row: SL_1 to SL_5 transfer, Bottom row: SL_2 to SL_5 transfer.

Looking at the dynamics around L_1/L_2, it has been derived that when the sail is oriented perpendicular to the Sun-sail line ($\alpha = 0$), both equilibrium points, and all the invariant objects around them, are shifted towards the Sun. The local stable and unstable manifolds display a similar qualitative behavior, but as we leave the vicinity of the equilibrium point, the dynamics experiences significant changes. For instance, in the classical (no solar sail) circular restricted three body problem (CRTBP) a branch of the L_1 unstable manifolds extends towards the L_4 neighborhood, while the other branch gets trapped around the Earth.

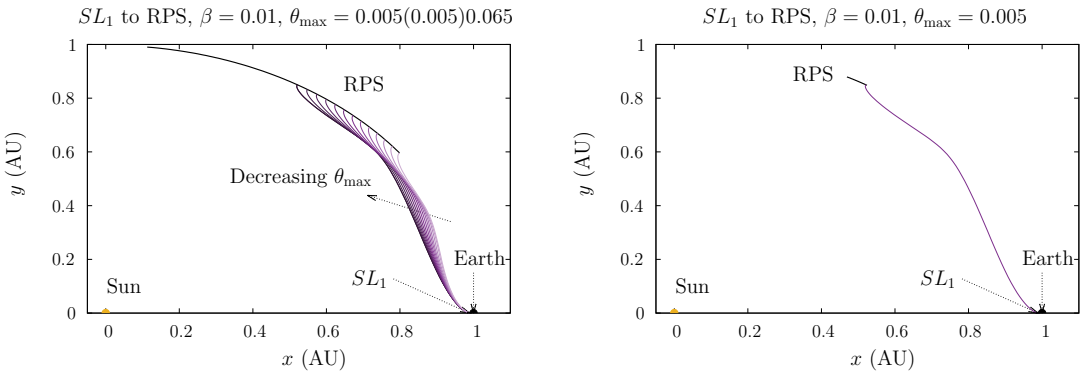

Figure 16: Time-optimal transfers from SL_1 to SL_4 stability region with $\beta = 0.01$ for different values for $\theta_{\max}$. Right: transfers for $\theta_{\max} = [0.065, 0.06, 0.055, \ldots 0.005]$, Left: transfer for $\theta_{\max} = 0.005$.

This impedes the design of transfer trajectories to L_5 using the invariant manifold of L_1. But it is remarkable that, as the sail lightness number increases, the branch that was trapped close to the Earth for $\beta = 0$ now manages to escape, providing transfers towards the L_5 neighborhood. Moreover, when the sail orientation changes, the manifold behavior becomes richer and we can take advantage of that.

Concerning the dynamics around L_4/L_5, since these are totally elliptic equilibria for the CRTBP, there is a region of practical stability around them. That is, orbits starting close enough to L_4/L_5 with zero synodical velocity will remain close to these equilibria for extremely long times. Hence, no station-keeping strategies are required. It has been shown that this behavior is preserved once the effect of SRP is added. We have studied the variation of the size of this region as β varies, and also how orbits, that start there, evolve over time. Hence, it makes sense to define a target region inside the RPS that can be written in closed form depending on the solar sail lightness number.

Combining the non-linear dynamics around L_1/L_2 and L_4/L_5 for $\beta \neq 0$ and $\alpha \neq 0$, different two-maneuver trajectories that transfer from one region to the other can be found. The idea is to match a trajectory leaving the displaced SL_1 and SL_2 equilibria along the unstable manifolds with a fixed sail orientation α_0 with a trajectory reaching the RPS at the displaced SL_4/SL_5 with another fixed sail orientation α_1. The change from one orientation to the other is performed at a Poincaré section at the mid-distance between the two points ($\Sigma_1 = \{y = \pm(x+\mu)/\sqrt{3}\}$). Using this simple approach we have been able to find, for $\beta = 0.01$, transfer trajectories joining all of the different regions: (a) from SL_1 to RPS at SL_4, (b) from SL_1 to RPS at SL_5, (c) from SL_2 to RPS at SL_4 and (d) from L_2 to RPS at L_5. From all the trajectories that have been explored, a larger variety of transfer options has been found starting from SL_1 towards both SL_4/SL_5 RPS, than starting from SL_2. Moreover, in general, the transfer times from SL_1 are smaller than from SL_2, although these trajectories are not time-optimal, as they have been found using a simple shooting method.

Therefore, using these manifold-type trajectories as initial guess in a direct pseudospectral optimization method, time-optimal transfers between the SL_1/SL_2 points and the RPS at SL_4/SL_5 have been found. For $\beta = 0.01$, the transfer times range between 669 and 1430 days. All transfers converged to a solution where the sailcraft enters the RPS at the point closest to Earth as this constitutes the shortest path. As such, improvements in the time of flight with respect to the initial guess of 1.7% to 59.9% have been achieved, depending on which of the four transfers is considered. The largest improvement of 59.9% is achieved for the transfer from SL_2 to SL_4 for which manifold-type trajectories can only be found by passing by the L_5 point, while the time-optimal solution shows a direct transfer between SL_2 and SL_4. Finally, it has been shown that by increasing the lightness number from a near-term value of $\beta = 0.01$ to a maximum far-term value of $\beta = 0.05$, further reductions in the time of flight of 44.4% to 67.2% to 320 - 538 days can be achieved.

Acknowledgments

The research by AF has been supported by the Spanish grant MTM2015-67724-P (MINECO/FEDER) and the Catalan grant 2014 SGR 1145. The research by NM has been supported by the Spanish grant MTM2016-80117-P (MINECO/FEDER) and the Catalan grant 2017 SGR 1374.

NM acknowledges the support of the ERC project COMPASS (Grant agreement No 679086).

JH acknowledges the support of the Marie Skłodowska-Curie Individual Fellowship 658645 - S4ILS: Solar Sailing for Space Situational Awareness in the Lunar System.

The authors would also like to thank J. Timoneda for the maintenance task of the computing facilities of the Dynamical System Group and the Facultat de Matemàtiques i Informàtica of the Universitat de Barcelona, that have largely been used in this work.

References

[1] V. M. Becerra. Solving complex optimal control problems at no cost with psopt. In *2010 IEEE International Symposium on Computer-Aided Control System Design*, pages 1391–1396, September 2010.

[2] B. Betts, B. Nye, E. Greeson, J. Vaughn, R. Chute, D.A. Spencer, R.W. Ridenoure, R. Munakata, S.D. Wong, A. Diaz, D.A. Stetson, J.D. Foley, J.M. Bellardo, , and B. Plante. Lightsail 1 mission results and public outreach strategies. In *4th International Solar Sailing Symposium*, Kyoto, Japan, January 2017.

[3] B. Dachwald, W. Seboldt, M. Macdonald, G. Mengali, A.A. Quarta, C.R. McInnes, L. Rios-Reyes, D.J. Scheeres, B. Wie, M. Görlich, et al. Potential Solar Sail Degradation Effects on Trajectory and Attitude Control. In *AAS/AIAA Astrodynamics Specialists Conference*, 2005.

[4] A. Farrés. *Contribution to the Dynamics of a Solar Sail in the Earth-Sun System.* PhD thesis, Universitat de Barcelona, 2009.

[5] A. Farrés. Catalogue on the dynamics of a solar sail around L_1 and L_2. In *Proceedings of the 4th International Symposium on Solar Sailing*, Kyoto, Japan, January 2017.

[6] A. Farrés. Transfer orbits to L_4 with a solar sail in the earth-sun system. *Acta Astronautica*, 137:78–90, August 2017.

[7] A. Farrés and À. Jorba. On the high order approximation of the centre manifold for ODEs. *Discrete and Continuous Dynamical Systems - Series B (DCDS-B)*, 14:977–1000, October 2010.

[8] A. Farrés and À. Jorba. Periodic and quasi-periodic motions of a solar sail around the family SL_1 on the Sun-Earth system. *Celestial Mechanics and Dynamical Astronomy*, 107:233–253, 2010.

[9] A. Farrés and À. Jorba. Artificial equilibria in the RTBP for a solar sail and applications. In Gerard Gómez and Josep J. Masdemont, editors, *Astrodynamics Network AstroNet-II*, pages 73–89, Cham, June 2016. Springer International Publishing.

[10] A. Farrés and N. Miguel. Solar sailing at the L_4/L_5 libration points. In *AAS/AIAA Astrodynamics Specialist Conference*, August 2017.

[11] R. L. Forward. Statite: A spacecraft that does not orbit. *Journal of Spacecraft*, 28(5):606–611, 1990.

[12] G. Gómez, À. Jorba, J. Masdemont, and C. Simó. *Dynamics and Mission Design Near Libration Points - Volume IV: Advanced Methods for Triangular Points.*, volume 5 of *World Scientific Monograph Series in Mathematics*. World Scientific, 2001.

[13] S. Gong and J. Li. Solar sail heliocentric elliptic displaced orbits. *J. of Guidance, Control, and Dynamics*, 37(6):2021–2025, 2014.

[14] N. Gopalswamy, J.M. Davila, O.C. St. Cyr, E.C. Sittler, F. Auchère, T.L. Duvall, J.T. Hoeksema, M. Maksimovic, R.J. MacDowall, A. Szabo, and M.R. Collier. Earth-affecting solar causes observatory (easco): A potential international living with a star mission from sun-earth l5. *Journal of Atmospheric and Solar-Terrestrial Physics*, 73(5):658 – 663, 2011.

[15] A. Griewank, D. Juedes, and J. Utke. Algorithm 755: Adol-c: A package for the automatic differentiation of algorithms written in c/c++. *ACM Transactions on Mathematical Software*, 22(2):131–167, 1996.

[16] A. Heaton, N. Ahmad, and K. Miller. Near earth asteroid scout solar sail thrust and torque model. In *4th International Symposium on Solar Sailing*, Kyoto, Japan, 2017.

[17] A. Heaton and A. Artusio-Glimpse. An Update to the NASA Reference Solar Sail Thrust Model. In *AIAA SPACE 2015 Conference and Exposition*, AIAA SPACE Forum. American Institute of Aeronautics and Astronautics, aug 2015.

[18] J. Heiligers, B. Diedrich, B. Derbes, and C.R.McInnes. Sunjammer: Preliminary end-to-end mission design. In *2014 AIAA/AAS Astrodynamics Specialist Conference*, August 2014.

[19] J. Heiligers, T.D. van den Oever, M. Ceriotti, P. Mulligan, and C.R. McInnes. Continuous planetary polar observation from hybrid pole-sitters at venus, earth, and mars. In *4th International Symposium on Solar Sailing*, Kyoto, Japan, 2017.

[20] J. Heliigers, G. Mingotti, and C.R. McInnes. Optimal solar sail transfers between halo orbits of different sun-planet systems. *Advances in Space Research*, 55:1405–1421, 2015.

[21] L. Johnson, R. Young, E. Montgomery, and D. Alhorn. Status of solar sail technology within nasa. *Advances in Space Research*, 48(11):1687 – 1694, 2011. SOLAR SAILING: CONCEPTS, TECHNOLOGY, AND MISSIONS.

[22] W.S. Koon, M.W. Lo, J.E. Marsden, and S.D. Ross. *Dynamical Systems, the Three-Body Problem and Space Mission Design.* Marsden Books, 2011.

[23] J.S.W. Lamb and J.A.G. Roberts. Time-reversal symmetry in dynamical systems: a survey. *Physica D*, 112:1–39, 1998.
[24] P. Llanos, J.K. Miller, and G.R. Hintz. Mission and navigation desing of integrated trajectories to l4/l5 in the sun-earth system. In *Aerospace Research Central & American Institute of Aeronautics and Astronautics, Inc.*, Septembre 2012.
[25] M. Macdonald, G. Hughes, C. McInnes, A. Lyngvi, P. Falkner, and A. Atzei. Geosail: An elegant solar sail demonstration mission. *Journal of Spacecraft and Rockets*, 44:784–796, 2007.
[26] A. McInnes. Strategies for solar sail mission design in the circular restricted three-body problem. Master's thesis, Purdue University, August 2000.
[27] C.R. McInnes. *Solar Sailing: Technology, Dynamics and Mission Applications*. Springer-Praxis, 1999.
[28] C.R. McInnes, M. MacDonald, V. Angelopolous, and D. Alexander. GEOSAIL: Exploring the Geomagnetic Tail Using a Small Solar Sail. *Journal of Spacecraft and Rockets*, 38(4):622–629, jul 2001.
[29] C.R. McInnes, A.J.C. McDonald, J.F.L. Simmons, and E.W. MacDonald. Solar sail parking in restricted three-body system. *Journal of Guidance, Control and Dynamics*, 17(2):399–406, 1994.
[30] C.R. McInnes and F.L. Simmons. Solar sail halo orbits i: Heliocentric case. *J. of Spacecraft and Rockets*, 29(4):466–471, 1992.
[31] G. Mengali, A. Quarta, C. Circi, and B. Dachwald. Refined Solar Sail Force Model with Mission Application. *Journal of Guidance, Control, and Dynamics*, 30(2):512–520, mar 2007.
[32] G. Mengali, A. Quarta, and V. Lappas. Optimal Steering Law for the GeoSail Mission. *Journal of Guidance, Control, and Dynamics*, 30(3):876–879, may 2007.
[33] A. Peloni, M. Ceriotti, and B. Dachwald. Solar-sail trajectory design for a multiple near-earth-asteroid rendezvous mission. *Journal of Guidance, Control, and Dynamics*, 39:2712–2724, 2016.
[34] M.B. Sevryuki. *Reversible Systems*. Springer-Verlag, Berlin, 1986.
[35] R. Shood and K. Howell. L_4, L_5 solar sail transfers and trajectory design: Solar observations and potential earth trojan exploration. In *26th AAS/AIAA Space Flight Mechanics Meeting*, February 2016.
[36] C. Simó. Boundaries of stability. Slides.
[37] C. Simó, P. Sousa-Silva, and M. Terra. Practical stability domains near $L_{4,5}$ in the restricted three-body problem: some preliminary facts. In *Progress and challenges in dynamical systems*, volume 54 of *Springer Proc. Math. Stat.*, pages 367–382. Springer, Heidelberg, 2013.
[38] A. Sobey and T. Russell Lockett. Design and development of nea scout solar sail deployer mechanism. In *Proceedings of the 43th Aerospace Mechanisms Symposium*, NASA Ames Research Center, May 2016.
[39] T. Svitek, B. Nye, J. Cantrell, and B. Betts. Voyage continues - lightsail-1 mission by the planetary society. In *61st International Astronautical Congress*, Prague, Czech Republic, 2010.
[40] V. Szebehely. *Theory of orbits. The restricted problem of three bodies*. Academic Press, 1967.
[41] Y. Tsuda, O. Mori, R. Funase, H. Sawada, T. Yamamoto, T. Saiki, T. Endo, K. Yonekura, H. Hoshino, and J. Kawaguchi. Achievement of ikaros – japanese deep space solar sail demonstration mission. *Acta Astronautica*, 82(2):183 – 188, 2013. 7th IAA Symposium on Realistic Advanced Scientific Space MissionsAosta, Italy, July 2011.
[42] G. Vulpetti, C. Circi, and T. Pino. Coronal mass ejection early-warning mission by solar-photon sailcraft. *Acta Astronautica*, 140:113 – 125, 2017.
[43] A. Wchter and L. T. Biegler. On the implementation of an interior-point filter line-search algorithm for large-scale nonlinear programming. *Mathematical Programming*, 106(1):22–57, 2006.
[44] J.L. West. The geostorm warning mission: Enhanced opportunities based on new technology. In *14th AAS/AIAA Spaceflight Mechanics Conference*, 2004.